

Polarization Properties and Magnetic Field Structures in the High-Mass Star-Forming Region W51 Observed with ALMA

Patrick M. Koch¹, Ya-Wen Tang¹, Paul T.P. Ho^{1,2}, Hsi-Wei Yen³, Yu-Nung Su¹, and Shigehisa Takakuwa^{4,1}

¹*Academia Sinica, Institute of Astronomy and Astrophysics, Taipei, Taiwan*

²*East Asian Observatory (EAO), 660 N. Aohoku Place, University Park, Hilo, Hawaii 96720, USA*

³*European Southern Observatory (ESO), Karl-Schwarzschild-Str. 2, D-85748 Garching, Germany*

⁴*Department of Physics and Astronomy, Graduate School of Science and Engineering, Kagoshima University, 1-21-35 Korimoto, Kagoshima, Kagoshima 890-0065, Japan*

pmkoch@asiaa.sinica.edu.tw

ABSTRACT

We present the first ALMA dust polarization observations towards the high-mass star-forming regions W51 e2, e8, and W51 North in Band 6 (230 GHz) with a resolution around $0''.26$ ($\sim 5\text{mpc}$). Polarized emission in all three sources is clearly detected and resolved. Measured relative polarization levels are between 0.1% and 10%. While the absolute polarization shows complicated structures, the relative polarization displays the typical anti-correlation with Stokes I , though with a large scatter. Inferred magnetic (B) field morphologies are organized and connected. Detailed substructures are resolved, revealing new features such as cometary-shaped B-field morphologies in satellite cores, symmetrically converging B-field zones, and possibly streamlined morphologies. The local B-field dispersion shows some anti-correlation with the relative polarization. Moreover, lowest polarization percentages together with largest dispersions coincide with B-field convergence zones. We put forward $\sin\omega$, where ω is the measurable angle between a local B-field orientation and local gravity, as a measure of how effectively the B-field can oppose gravity. Maps of $\sin\omega$ for all three sources show organized structures that suggest a locally varying role of the B-field, with some regions where gravity can largely act unaffectedly, possibly in a network of narrow magnetic channels, and other regions where the B-field can work maximally against gravity.

Subject headings: ISM: individual objects: (W51 e2, W51 e8, W51 d, W51 North, W51 IRS2, W51 A) – ISM: magnetic fields –polarization – stars: formation

1. Introduction

The giant molecular cloud W51 is among the most massive star-forming regions in our Galaxy. The W51 complex is further unique as it is located in a region with little foreground and background contamination. Ginsburg (2017) gives a recent observational review. The major regions within W51 are W51 A, B, and C. The two most luminous high-mass protostars, W51 e2 and W51 North, are located in the W51 A region which has a luminosity equivalent to a star cluster of 5,000 to 10,000 M_{\odot} . W51 e2 together with e8 is located along a molecular ridge at a parallax distance around 5.41 kpc (Sato et al. 2010). Parallax measurements towards W51 North yield about 5.1 kpc (Xu et al. 2009). W51 contains an aggregation of HII regions (Westerhout 1958; Martin 1972; Mehringer 1994) and masers detected in several molecular lines (OH in W51 e2, e8, and North, (Etoka et al. 2012); H₂O in e2, e8, and North (Genzel et al. 1981; Imai et al. 2002; Eisner et al. 2002); CH₃OH in e2, e8, and North (Phillips & van Langevelde 2005; Etoka et al. 2012); SiO and NH₃ in W51 North (Morita et al. 1992; Eisner et al. 2002; Brown & Cragg 1991; Gaume et al. 1993; Henkel et al. 2013). W51 A, due to being very bright in the millimetre wavelength range, has been extensively studied with a variety of molecular lines. Evidence for infall and / or accretion around W51 e2 is reported in Ho & Young (1996); Zhang & Ho (1997); Zhang et al. (1998); Young et al. (1998); Sollins et al. (2004). A possible rotation with a spinning-up motion is discussed in Zhang & Ho (1997); Zhang et al. (1998). Observations of the hydrogen recombination line H53 α led to the interpretation of a rotational ionized accretion flow around the ultra-compact HII region in e2 (Keto & Klaassen 2008). Later higher-resolution observations by Shi et al. (2010a,b); Goddi et al. (2015, 2016) reveal that e2 fragments at least into two sources, e2-west (a hyper-compact HII region) and e2-east (a hot molecular core), suggesting that the accretion is possibly onto these smaller-scale cores. W51 e8, south of e2 at a projected distance around 0.3 pc, appears to be in a common larger-scale 0.5 pc envelope together with e2 (Lai et al. 2001; Tang et al. 2009). Infall signatures towards e8 are detected in NH₃ (Ho & Young 1996; Zhang & Ho 1997; Zhang et al. 1998) and in CS (Zhang et al. 1998), indicating an early evolutionary stage. Towards W51 North, infall motions are detected in SO₂ (Sollins et al. 2004) and CN (Zapata et al. 2008). At a higher angular resolution of 0''.4, Zapata et al. (2009) observed an infalling ring-like structure in SO₂. The orientation of the molecular outflow traced in SiO (5–4) (150°, Zapata et al. (2009)) is similar to the orientation derived from proper motions of H₂O masers (105° to 140°, Eisner et al. (2002); Imai et al. (2002)). High-resolution continuum observations at 0''.7

resolve W51 North in at least four smaller cores along an east-west direction south of the cometary shell-like HII region W51 d (Tang et al. 2013). Recent ALMA observations with a resolution of 1000 au in multiple lines do not reveal unambiguous signatures of infall in e2, e8, or North, but this is likely caused by observational limitations rather than a non-existence of infall motion (Ginsburg et al. 2017).

The focus of the present paper is to study the role of the magnetic (B) field with the Atacama Large Millimeter/submillimeter Array (ALMA) at a physical scale around 5 mpc in W51 e2, e8, and North. To that purpose we are making use of dust polarization observations. At the densities and scales probed with our resolution in these high-mass star-forming regions, dust grains are expected to be coupled to the B-field, aligned with their shorter axis parallel to the B-field. Their emission at (sub-)millimetre wavelength is, thus, polarized perpendicular to the B-field lines (Cudlip et al. 1982; Hildebrand et al. 1984; Hildebrand 1988; Lazarian 2000; Andersson et al. 2015). This dust alignment is likely made possible through radiative torques (Draine & Weingartner 1996, 1997; Lazarian 2000; Cho & Lazarian 2005; Lazarian & Hoang 2007; Hoang & Lazarian 2016).

The W51 e2/e8 ridge has already been the focus of dust polarization observations in order to map and study the B-field. Berkeley-Illinois-Maryland-Association (BIMA) radio telescope array observations at 1.3 mm with a resolution $\theta \sim 3''$ show an elongated one-parsec long envelope around e2/e8 with the B-field mostly oriented perpendicular to the envelope’s longer axis (Lai et al. 2001). At the location of the e2 core there is noticeably less or no polarization detected with this ~ 0.1 pc resolution. Higher-resolution observations with the Submillimeter Array (SMA) clearly resolved a radial-like pinched B-field morphology precisely at the location of e2 and a more stretched morphology in e8 with $\theta \sim 0''.7$ at $870\mu\text{m}$ (Tang et al. 2009). Comparing gravitational force and B-field tension and noticing that both the e2 and e8 core show signatures of infall, upper limits for their B-field strengths are estimated to be < 19 mG (e2) and < 8 mG (e8), respectively (Tang et al. 2009). The large-scale B-field in the plane of the sky, pervading the 0.5-pc envelope, is estimated to be ~ 1 mG from the Chandrasekhar-Fermi (Chandrasekhar & Fermi 1953) method in Lai et al. (2001). Subsequently, W51 e2 served as a testbed for a newly developed technique – the polarization-intensity gradient method – to measure local magnetic field strengths (Koch, Tang & Ho 2012a,b). A clear increase in field strengths is measured from ~ 1 mG in the core’s peripheral zones to a central value around 20 mG. Etoke et al. (2012) quote a B-field strength of 2-7 mG from OH masers in e2 which is similar to field strengths measured in other compact HII regions detected through Zeeman observations of OH masers (a few mG up to ~ 20 mG, Fish & Reid (2007)). An analysis of the local magnetic field-to-gravity force ratio shows a clear drop towards the center of e2, indicating that the B-field is largely overwhelmed by gravity in the central region while the field can still provide resistance (force

ratio larger than unity) in the northwestern area (Koch, Tang & Ho 2012a). An identical picture is seen on larger scales, both in between W51 e2/e8 and W51 North, and in between W51 e2 and e8 with a larger field resistance against gravity in between the cores and gravity dominating at the locations of the cores (Koch, Tang & Ho 2012b).

W51 North was the target of a systematic study to probe the change in B-field morphologies (Tang et al. 2013) from a 3-pc envelope surface layer (JCMT/SCUPOL at $850\mu\text{m}$, Chrysostomou et al. (2002); Matthews et al. (2009)) to the pc-scale molecular cloud probed with the CSO/Hertz at $350\mu\text{m}$ (Dotson et al. 2010) down to the core envelope and core resolved with the SMA at the 0.1-pc scale (Tang et al. 2013). The systematic change from a close-to-uniform larger-scale B-field, to a symmetric from north and south channelling field morphology, down to a pulled-in hourglass-like B-field is also reflected in a tightening correlation between emission gradients and field orientations (Tang et al. 2013) which is explained by gravity more and more dominating over the B-field (Koch, Tang & Ho 2013). This finding was later confirmed in a large 50-source sample with the SMA and the CSO data in Koch et al. (2014). In W51 North, field-to-gravity force ratios are small (around 0.5) on average, but grow to values larger than unity outside of the core regions (Tang et al. 2013).

This paper is organized as follows. Section 2 describes our ALMA observations. Maps of dust continuum, polarized emission and B-field morphologies are presented in Section 3. We discuss the connection between polarization and B-field structures, together with a comparison to larger-scale data of the envelope of W51 e2/e8 and North from the SMA, in Section 4. This section further debates B-field versus gravity with a new proposed measure. Summary and conclusion are given in Section 5.

2. Observations

The project was carried out with the ALMA Band 6 receiver during the Early Science (Cycle 2, project "2013.1.00994.S"). Observations were done in three execution blocks (EBs) on July 18, 2015. The three EBs were calibrated separately in flux, bandpass and gain. Polarization calibration was performed after merging the three calibrated EBs following the standard polarization calibration for ALMA¹. A detailed analysis of the instrumental polarization in Band 6 is given in Nagai et al. (2016) which conclude that linear polarization at a level of $< 0.1\%$ is detectable. The array included 38 antennas with (projected) baselines ranging from 13 m to 1492 m. The four basebands were set in FDM mode (3840 channels for 1.875 GHz with a resolution of 488 kHz). The calibration (bandpass, phase,

¹ CASA guide https://casaguides.nrao.edu/index.php/3C286_Polarization

amplitude, flux) was performed using CASA² v4.5.0. J1924-2914 and J1751+0939 were used for bandpass, and J1922+1530 for phase calibration. With a flux of 0.175 Jy at 232.9 GHz, J1922+1530 also provided the flux scale with the reference flux calibrator Titan. The polarization calibrator was J1924-2914, which was measured to have a polarization fraction of 2.56% and a polarization position angle of 45.6°, in agreement with other ALMA measurements. W51 was observed with three separate pointings, with phase centers on e2, e8 and North on $(\alpha, \delta)_{\text{J2000.0}} = (19:23:43.95, 14:30:34.00)$, $(19:23:43.90, 14:30:27.00)$ and $(19:23:39.95, 14:31:05.50)$, respectively. The images presented here are with natural weighting, which gives a synthesized beam resolution $\theta \sim 0''.28 \times 0''.26$ with an orientation of 33°. The sensitivities (1σ) are 6 mJy/beam (e2, e8) and 1.4 mJy/beam (North) for Stokes I , 0.15 mJy/beam (e2, e8) and 0.08 mJy/beam for Stokes Q , and 0.19 mJy/beam (e2, e8) and 0.10 mJy/beam for Stokes U (Figure 1 and 2). Since polarization measurements $I_p = \sqrt{Q^2 + U^2} > 0$ have a positive bias (while both Q and U can be negative), we debias in the high signal-to-noise regime ($I_p \geq 3\sigma_p$) with $I_p = \sqrt{Q^2 + U^2 - \sigma_{Q,U}^2}$, where $\sigma_Q \approx \sigma_U$ are the noise levels in Q and U (Leahy 1989; Wardle & Kronberg 1974). For all results displayed in this paper we impose the two simultaneous conditions of having Stokes $I \geq 3\sigma$ and $I_p \geq 3\sigma_p$. Resulting median uncertainties and standard deviations of uncertainties for polarization percentages $p = I_p/I$ are 0.21% and 0.15% for W51 e2, 0.28% and 0.16% for W51 e8, and 0.16% and 0.13% for W51 North. Maximum and minimum uncertainties are 0.50% and 0.02%. Median uncertainties and standard deviations of uncertainties for the orientations of polarization position angles are 2.5° and 2.1° for e2, 2.7° and 2.1° for e8, and 3.0° and 2.4° for North. Maximum uncertainties are around 9°.

For comparison, we also present new larger-scale SMA maps combining data from the subcompact array configuration (described originally in Tang et al. (2013) for W51 North) and the compact array configuration (described originally in Zhang et al. (2014) for W51 e2, e8, and W51 North). Additionally, unpublished data on W51 e2 and e8 from subcompact array observations are added. The resulting images have $\theta \sim 2''.13 \times 1''.88$ with an orientation of 28°, which captures the envelope scale and the previously unseen connection between W51 e2 and e8 (panel (a) and (f) in Figure 1 and 2).

²<http://casa.nrao.edu/>

3. Results

3.1. 230 GHz Dust Continuum

The continuum emission is well detected and resolved at a $0''.26$ resolution towards W51 e2, W51 e8 and W51 North (Figures 1 and 2). The total detected continuum emission at 230 GHz in Stokes I is 4.0, 3.7 and 6.8 Jy for W51 e2, e8 and North, respectively.

The W51 e2 core is resolved into 4 sub-cores (Table 1). The flux densities of these dense cores are determined by two-dimensional Gaussian fits to be 2.54, 1.04, 0.22 and 0.10 Jy for W51 e2-E, e2-W, e2-NW and e2-N, respectively, and there is faint emission (0.2 Jy) in between these cores. The W51 e2 core has also been resolved at 1.3 mm by Shi et al. (2010a) using the SMA with $\theta \sim 1''.1$. Their reported flux densities are 2.15 ± 0.12 , 0.62 ± 0.12 and 0.73 ± 0.08 Jy for W51 e2-E, e2-NW and e2-N, respectively. Our newly reported flux densities are within the 3σ uncertainty levels of the ones in Shi et al. (2010a). We note that this difference can be explained by the coarser angular resolution of the SMA observations with respect to the separations of these sub-cores. In addition, in our ALMA data, there is no detection at the location of W51 e2-N reported in Shi et al. (2010a). Instead, there is a sub-core detected in the presented ALMA data $0''.5$ west of W51 e2-N. We attribute this emission to W51 e2-N in Shi et al. (2010a) and hence, the nomenclature is kept unchanged. This shift in position is a result of the interferometric filtering effect, where the emission from relatively smooth and extended structures will be filtered out, and the structures revealed by ALMA have fewer artefacts due to a more complete uv-coverage.

The W51 e8 region is resolved into two cores, e8-N and e8-S, with some additional faint emission in the south of e8-S. The flux densities are 2.65 Jy and 0.34 Jy for the e8-N and e8-S core, respectively.

The continuum emission towards the W51 North region shows several cores aligned in an east-west direction. These cores have been resolved and reported in Tang et al. (2013). The SMA2 core is now further resolved into a new core to its southwest (N2) and a likely additional emerging peak to its east (SMA2-E). Hereafter, W51 N1 refers to SMA1, W51 N2 to the newly resolved peak southwest of SMA2, W51 N3 to SMA3 and W51 N4 to SMA4. The flux densities are 2.88, 1.49, 0.96, 0.89, and 0.59 Jy for N1, SMA2-E, N2, N3, and N4, respectively (Table 1).

3.2. Polarization

Polarized emission above 3σ is seen and resolved with ALMA at 230 GHz in W51 e2, e8, and W51 North (panel (d), (e), and (h) in Figure 1). Polarization holes or de-polarization zones in the earlier observations with the SMA at 345 GHz ($\theta \sim 0''.7$, here reproduced from Tang et al. (2009) in panel (b), (c), and (g) in Figure 1) are now resolved with ALMA. It is obvious from Figure 3 that the *absolute polarized emission* I_p does not simply scale with Stokes I . W51 e2, e8, and W51 North show high- and low-emission zones and spots in I_p that appear to have no counterparts in I . This is clearly seen in the plots I_p versus I (Figure 13, Appendix) that show no correlation but a broad scatter between these two observables. We note that this joint interpretation of I with I_p assumes that both the total intensity and the polarized signal result from the same structure along the line of sight within a synthesized beam resolution. This means that no significant contamination from background, foreground, or any intervening structures should be present.

W51 e2: Zones of decreasing and minimum polarized emission are centered on e2-W, across e2-E along a northeast-southwest direction, and away from the e2-E emission peak along a narrow straight line towards northwest (Figure 3). A peak is detected east of e2-E and in between the east and west core. The e2-NW satellite core reveals itself with a stripe of minimum polarization along an east-west direction, a growing signal towards the east and two maxima in the north and south, displaying an almost perfect north-south symmetry. This symmetry is also reflected in the magnetic field morphology (Section 3.3, Figure 2).

W51 e8: Absolute polarized emission peaks are seen west of the e8-N peak, in between e8-N and e8-S, and east of e8-S at the lowest Stokes I emission contour. Zones of minimum polarization appear east of the e8-N peak and to its north-west. Both the northern and southern end of e8-S show low-level absolute polarization.

W51 North: Peaks in absolute polarized emission are detected north and south of the core N2 around R.A. offset 0. To a smaller extent, two additional local maxima are seen north and south of the core N1 around R.A. offset 1.5. The remaining cores and connections in between them are mostly weakly polarized around 1 mJy/beam or less, with a few patches that are slightly more polarized up to about 2 mJy/beam.

Unlike the above *absolute polarization*, the *relative polarization* $p = I_p/I$ shows systematic trends where p grows with decreasing Stokes I (Figures 1, 4). This is the typically observed anti-correlation of *relative polarization* versus Stokes I , i.e., p versus I/I_{max} if normalized by the maximum Stokes I value, as e.g., in Tang et al. (2009). Without any exception, all cores in W51 e2, e8 and North show local minima in p at their Stokes I emission peaks. Similarly, maximal polarization percentages are always associated with the lowest

contours in I . Nevertheless, a constant I contour can show a significant variation in relative polarization (Figure 4). This means that symmetries in I are not necessarily preserved in p , as e.g., evident in e2-E and N2. This naturally leads to a scatter in the p versus I correlation. This scatter is relatively broad over almost one order of magnitude (Figure 5). It, thus, likely hints a dependence on additional physical parameters that are not captured in this simple anti-correlation. Polarization percentages go over two orders of magnitude, ranging from around 0.1% to 10% in all sources (Figure 5). The anti-correlation can be fit with power-laws with indices -1.02 (e2), -0.84 (e8), and -0.84 (North). Similar slopes are seen in the larger-scale SMA 345 GHz (850 μm) data (Section 4.3) and in an SMA-BIMA comparison for e2/e8 (Tang et al. 2009) and in a comparison with CSO (at 350 μm) and JCMT (at 850 μm) observations for North (Tang et al. 2013). A possible connection between the spatially varying polarization percentage p and the observed B-field morphologies is discussed in Section 4.1.

3.3. Magnetic Field Morphologies

Magnetic (B) field morphologies are clearly detected, revealing organized, coherent and connected structures. Furthermore, substructures in and in between individual cores, and shaped B-field morphologies in satellite cores can now be identified (Figure 2). In this section, B-field orientations are generated by rotating the originally detected polarization orientations in Figure 1 by 90° . B-field segments are all displayed with equal lengths, neglecting information about relative polarization (Section 3.2).

W51 e2: Overall, most of the B-field segments are pointing towards the main emission peak e2-E (panel (d) in Figure 2). In the closer vicinity of the e2-E peak, the segments are becoming almost radial-like. Overall, the field structure around e2-E resembles a dragged-in morphology. Around e2-W, the field segments in the south-western peripheral area are bent towards the e2-W emission peak, while the remaining surrounding segments still point towards the main peak e2-E, leaving straight segments along an east-west direction between e2-E and e2-W. This possibly indicates that e2-W is pulled towards the more massive e2-E core. The main core e2-E displays two additional features. Firstly, the previous depolarization stripe along the northeast-southwest direction in the SMA observation (panel (b) in Figure 2) is resolved, clearly showing a continuation of B-field segments that now appear to converge from above and below towards a mid-plane along this stripe. Secondly, perpendicular to this, B-field segments align along a straight northwest-southeast axis. This is particularly obvious in the northern upper plane with field segments converging symmetrically from both east and west towards this central straight axis. Finally, the satellite core

e2-NW appears with a cometary- or bow-shock-shaped B-field morphology. This core hints a pinched field structure in the west and a curved bow-shock structure in the east with a north-south symmetry. These features might suggest that e2-NW is passing through the ambient (lower-density) medium from west to east.

W51 e8: The more elongated e8 structure is clearly detected and further resolved into the main core e8-N and e8-S (panel (e) in Figure 2). The polarization coverage is significantly improved as compared to the earlier SMA map (panel (c) in Figure 2). While the western side of e8-N displays B-field segments that appear oriented towards the emission peak, the eastern and particularly the northeastern side indicate field lines that are bending away, more closely aligning with a north-south axis. The smaller core e8-S hints a cometary field morphology. Although not as obvious as e2-NW, it hints identical features with possibly pinched field lines in its southern end and more curved cometary-shaped segments in the northern part. This is suggestive of e8-S being pulled north towards the more massive e8-N. This impression is further supported by the possibly streamlined B-field segments in the lower density bridge between the northern tip of e8-S and the southern tail of e8-N. This morphology – likely shaped by a streaming motion – might also be present at the northern and northeastern zones of e8-N, possibly indicating that the entire e8 is pulled north towards the more massive e2.

W51 North: This region harbours at least six cores, aligned along an east-west axis and almost uniformly spaced. Each core displays an organized magnetic field structure (panel (h) in Figure 2). The two most massive cores – N1 and N2 from east to west around R.A. offsets $1''.5$ and $0''$ – both exhibit B-field segments oriented towards their emission peaks. While N1 appears with a clearly pinched and complete hourglass B-field morphology, symmetric around a northwest-southeast axis, N2 only presents likely dragged-in field lines at its western end. In the east, the field segments appear to open up again, be more straight and possibly oriented towards the larger and more massive N1. Similar to e2-W and e8-S, this characteristic field morphology might be symptomatic for the less massive core (here, N2) being pulled towards the next more massive gravitational center (N1). In contrast to N1 and N2, N3 around R.A. offset $-2''$ clearly reveals field orientations that are dominantly not oriented towards its emission peak, except in the southwestern zone. Many of the B-field segments are largely north-south oriented but with a twist towards the east. This is particularly noticeable in the eastern extension of N3 that forms a bridge (around R.A. offset $-1''$) to N2 and where probably another core is embedded. This overall bending of the entire group of field segments could again indicate that N3, as a whole, is being dragged to the more massive N2. Finally, the smallest and least massive core N4 at the western end of W51 North (around R.A. offset $-3''$) possibly also shows a glimpse of field segments being oriented towards the next more massive N3 to the east, although some segments in the west also show a north-south

alignment and some tendency towards the emission peak.

4. Discussion

4.1. Polarization Structures and Magnetic Field Morphologies

The polarized emission – both absolute and relative to Stokes I (Figures 3 and 4) – is clearly not random but appears organized, though in a non-trivial way. Can this emission be understood together with the plane-of-sky projected B-field morphologies? Here, we explore correlations among the observables Stokes I , polarized emission I_p , polarization percentage $p = I_p/I$, and the local B-field dispersion \mathcal{S} . The latter one was recently probed on large data sets by *Planck* (Planck Intermediate Results XIX 2015; Planck Intermediate Results XX 2015) and BLASTPol (Fissel et al. 2016). The local B-field dispersion is defined as

$$\mathcal{S}(\mathbf{r}, r_{disp}) = \sqrt{\frac{1}{N} \sum_{i=1}^N [PA(\mathbf{r}) - PA(\mathbf{r} + \mathbf{r}_{disp,i})]^2}, \quad (1)$$

where PA is the position angle of an observed B-field segment at a location \mathbf{r} and i is counting neighboring B-field segments within an annulus $r_{disp} \geq |\mathbf{r}_{disp,i}|$ centered on \mathbf{r} . Figure 6 shows \mathcal{S} -maps, evaluated for $r_{disp} = 0''.2$, which measures the field dispersion in an area slightly larger than the synthesized beam $\theta \sim 0''.26$. This means that \mathcal{S} is capturing by how much a local field orientation changes with respect to its nearest four and next-nearest four neighbors. \mathcal{S} will select zones and display larger values where the B-field bends more rapidly or changes orientation abruptly. In W51 e2-E (Figure 6, upper left panel) the northeast-southwest mid-plane, towards which the field segments seem to converge from north and south, is clearly identified with larger dispersion values \mathcal{S} . Except this stripe, e2-E shows mostly small values, which is a consequence of its radial-like field morphology. An additional zone with clearly enhanced \mathcal{S} -values is in the northern low-emission region between e2-E and e2-W. This is again a zone where field segments converge symmetrically from east and west towards a central straight axis (Section 3.3). The \mathcal{S} -parameter also identifies the western side of the mid-plane in the satellite core e2-NW as a large-dispersion area. Similarly to e2-E, this reflects the mirror-symmetric field structures. The \mathcal{S} -map for e8-N/S is less prominent (Figure 6, upper right panel). Generally, B-field orientations appear to change less abruptly in the west (low values in \mathcal{S}) while the eastern half shows larger dispersion values. Similarly to e2-NW, \mathcal{S} highlights the southern end of e8-S, where the B-field might be locally dragged in, as an enhanced dispersion zone. Equally, the northern end of e8-S, where the curved cometary-like field structure is opening up, straightened and possibly pulled towards e8-N, also shows a patch of larger field dispersion. Finally, the possibly converging streaming

zone from southeast to the height of e8-N shows up as an elongated stretch with larger \mathcal{S} -values. W51 North (Figure 6, bottom panel) shows an overall more uniformly small B-field dispersion. Two zones of enhanced dispersion are identified symmetrically around N1, in its southeast and northwest. This coincides with the pinching direction of the hourglass-like B-field. Two additional large-dispersion regions are seen slightly off the peaks of N3 and N4. In summary, in all three regions, W51 e2, e8 and North, the \mathcal{S} -parameter is often capturing areas that a visual inspection identifies as *magnetic field convergence zones* (Section 3.3).

The spatial coincidence between lowest polarization fractions p (Figure 4) and largest dispersions \mathcal{S} (Figure 6) is visible in many cores, e.g., stripe across e2-E and e2-NW, wings on N1, and peaks and offsets in N3 and N4. Figure 7 shows the local B-field dispersion \mathcal{S} as a function of polarization percentage p . While a large scatter in \mathcal{S} is seen for peak polarizations, the smallest polarization percentages clearly converge towards the largest field dispersions. \mathcal{S} appears to be anti-correlated with p , with a lower envelope (that traces the minimum polarization as a function of dispersion) and with a scatter that increases with p . Lowest polarization occurs at maximum dispersion values while these are seen across the entire Stokes I range. \mathcal{S} appears, thus, only weakly, if at all, correlated with I (see Figure 13 in Appendix). This is observed for all three regions, e2, e8, and North. The drop in polarization p with increasing field dispersion can be interpreted as the cancellation of some polarization signal due to more rapid changes in the field orientations. Hence, this might indicate that the observed field structures in W51 at a scale of 5 mpc ($\theta \sim 0''.26$) are not yet resolved at those locations, but underlying more rapidly changing structures within our synthesized beam can be responsible for this anti-correlation. This same explanation holds for the observed anti-correlation between p and Stokes I (Section 3.2 and Appendix Figure 13), assuming that I is a fair tracer for the gas column density. Alternatively, an intrinsic lower grain alignment efficiency, due to varying densities and temperatures, might also explain these two anti-correlations. Our findings are in line with recent BLASTPol results for the Vela C molecular cloud (Fissel et al. 2016) where a two-variable power-law empirical model is derived to describe the anti-correlation between p and \mathcal{S} , and p and column density N on a scale of about 0.5 pc (observed at $500\mu\text{m}$ with a resolution around $2''.5$). A decrease of p with growing dispersion \mathcal{S} on even larger scales is also noted in Planck Intermediate Results XX (2015). Our observations, thus, indicate a continuation of these anti-correlations on large parsec scales down to mpc scales.

Finally, we notice that the absolute polarization I_p (Figure 3) and the local field dispersion \mathcal{S} (Figure 6) – although scattering in a broad band when comparing entire maps (Appendix, Figure 13) – appear with similar structures in certain regions. In particular, this is the case for e2-E and e2-NW, and e8 N/S where maximum values in \mathcal{S} always reflect minimum I_p values. The fact that no overall correlation is apparent, is likely because small

and medium dispersions seem to come with any values in I_p . This is especially the case for W51 North. While \mathcal{S} vs I_p seems to show a weaker less general correlation than \mathcal{S} vs p (Figure 7), the correlation tightens when limited to values around $I_{p,min}$ and \mathcal{S}_{max} . As such, it namely exactly identifies the *magnetic field convergence zones* which appear with large \mathcal{S} , and both small polarization percentage p and small absolute polarization I_p .

4.2. Gravity vs Magnetic Field: Local B-Field Resistance and Magnetic Channeling

Section 3.3 has presented novel B-field features resolved with the ALMA 0'26 observations, namely (1) cometary B-field morphologies in e2-NW and e8-S, (2) convergence zones with symmetrical field structures in e.g., e2-E, and (3) possibly streamlined field morphologies between e.g., e8-S and e8-N, and north of e8-N towards e2. These new features are now starting to give the impression of actually seeing the dynamics of flowing material imprinted on and / or by the magnetic field morphologies. Here, we are adding quantitative estimates that support this dynamical picture carved by these detailed B-field morphologies.

How important is the magnetic field in, e.g., e2-E, e2-W and e2-NW? In which cores can it still slow down gravitational infall, where is the field already overwhelmed by gravity, and might there be even local differences within the same core? We start our analysis from an ideal MHD force equation (e.g., Koch, Tang & Ho 2012a) that identifies the local direction of gravity through $\nabla\phi$ and the direction of the magnetic field tension force through \mathbf{n}_B . We impose the slight restriction that any change in the orthogonal field component is much smaller than the total field strength, i.e. $\frac{\Delta B_{\perp}}{B} \ll 1$. This will hold for any spatially slowly changing field functions³. In return, this then allows us to simplify and combine the magnetic field hydrostatic pressure and the field tension terms. With this, the force equation becomes (Koch, Tang & Ho 2012a):

$$\rho \left(\frac{\partial}{\partial t} + \mathbf{v} \cdot \nabla \right) \mathbf{v} = -\nabla P - \rho \nabla \phi + \frac{1}{4\pi} \frac{1}{R} B^2 \mathbf{n}_B, \quad (2)$$

where ρ and \mathbf{v} are the dust density and velocity, respectively. B is the magnetic field strength. P is the hydrostatic dust pressure. ϕ is the gravitational potential resulting from the total

³ On very small scales, this assumption might eventually fail for tangled magnetic fields if neighboring beams show large or abrupt changes in field orientations. There is, however, no indications of this to date from observed field morphologies. The ALMA data presented here also still show smooth and continuous changes in almost all locations. The local field dispersion \mathcal{S} (Section 4.1) quantifies this with overall small values.

mass contained inside the star forming region. ∇ denotes the gradient. The field tension force (last term on the right hand side) with the field curvature $1/R$ is directed normal to the field line along the unity vector \mathbf{n}_B .

Since we are interested in comparing gravity and B-field, we rewrite the above equation by projecting the direction of the field tension force onto the direction of gravity, i.e., $\mathbf{n}_B = \cos \omega \cdot \mathbf{n}_g + \sin \omega \cdot \mathbf{g}$, where \mathbf{g} is a unity vector along the local direction of gravity $\nabla\phi$, \mathbf{n}_g is the direction normal to it forming an orthonormal system with \mathbf{g} , and ω is the angle between the local direction of gravity⁴ $\nabla\phi$ and the local B-field orientation, measured in a range between 0 and 90° (Figure 8). Equation (2) can then be rewritten as

$$\rho \left(\frac{\partial}{\partial t} + \mathbf{v} \cdot \nabla \right) \mathbf{v} = -\nabla P - \rho |\nabla\phi| \mathbf{g} + \frac{1}{4\pi} \frac{1}{R} B^2 \sin \omega \mathbf{g} + \frac{1}{4\pi} \frac{1}{R} B^2 \cos \omega \mathbf{n}_g. \quad (3)$$

In this way, the influence of the magnetic field along the direction of gravity \mathbf{g} , i.e., its effectiveness opposing gravity, is quantified with the term $1/(4\pi R)B^2 \sin \omega$. In particular, the factor $\sin \omega$ defines the fraction of $1/(4\pi R)B^2$ that can work against gravity to slow down or prohibit infall, collapse, and any motion driven by gravity. $\sin \omega$ is zero if the B-field is aligned with the local direction of gravity. In this case, independent of the field strength, the B-field can not resist gravity. The magnetic field can maximally work against gravity if the field is orthogonal to gravity. Here, the precise effect will further depend on the field strength.

Figure 9 shows $\sin \omega$ -maps for the ALMA observations of W51 e2, e8, and North. It is evident that values are not random but appear in organized structures that can change with location. $\sin \omega$ averaged over the entire W51 e2 map is small with 0.40 and a standard deviation of 0.27. This indicates that e2, as an entity, is likely overwhelmed by gravity

⁴ Calculating the local direction of gravity is introduced in Koch, Tang & Ho (2012a). The observed dust emission *distribution* is assumed to represent the total mass *distribution* that generates the gravitational potential ϕ . In order to measure the angle ω , only the direction of the gravitational pull, $\nabla\phi$, is needed but not its magnitude. The total mass, linked to the dust emission through an a priori unknown dust-to-gas mass ratio, is not needed and hence, it suffices to only consider the dust distribution for this calculation. The resulting local direction of gravity at a specific location is then derived by summing up all the surrounding pixelized dust emission weighted by $1/r^2$ along the direction to each pixel, where r is the distance between that location and every surrounding pixel. In other words, every surrounding pixel is treated as a point mass that is exerting a gravitational pull on that specific location. The smallest scale that can be taken into account is given by the (synthesized) beam resolution. The largest size scale is defined by the largest distance to any detected emission. We note that larger diffuser scales (emission) are filtered out in the ALMA data but this is unlikely significantly affecting our results because (1) while already being weak, this emission is additionally less important due to a growing $1/r^2$ shielding; (2) the larger-scale emission often tends to be more symmetrically distributed, and resulting gravitational pulls can thus largely cancel out.

on the observed scales, with an overall small magnetic field resistance. e2-E displays some field resistance in the east that appears to grow towards the center. An additional zone of more significant B-field presence is in the north with $\sin \omega \sim 0.5$ or larger. Both zones occur at locations where the detected B-field orientations (panel (d) in Figure 2) are clearly more misaligned with the close-to-radial gravity directions which result from close-to-circular emission contours of the individual cores. The area with largest B-field resistance ($\sin \omega \sim 1$) is around and north of e2-W. In this zone, the B-field appears to be more tangential to the dust emission contours, possibly suggesting a pull towards e2-E and, therefore, a B-field opposing the local gravitational pull towards the center of e2-W. The satellite core e2-NW displays a north-south asymmetry with minimal $\sin \omega$ values in the north and values close to one in the south. This is opposite to the observed north-south symmetry in the cometary B-field morphology, and in both I_p and p (Figures 2, 3, 4). What likely drives this asymmetry is the massive e2-E/e2-W complex that is pulling e2-NW towards south. As a consequence, local gravity directions in the e2-NW core deviate from being simply radial towards its emission peak. This effect is most significant in the south, thus, leading to large misalignments ω between field orientations and gravity.

W51 e8 shows a very similar overall B-field effectiveness to oppose gravity with an average $\sin \omega$ value of 0.41 and a standard deviation of 0.29. e8-N dominantly reveals small values around 0.2-0.5, as expected from the likely pulled-in field morphology in these locations (panel (e) in Figure 2). The exception is the eastern side with values up to one. These highest values coincide with field segments that are more tangential to contours and the possible bending away from e8-N (Section 3.3). Except for a western triangular section with $\sin \omega \sim 0.7$, the elongated bridge between e8-N and e8-S mostly displays small values around 0.1-0.3. This is in agreement with the visual impression of a streamlined B-field morphology that is probably driven by the locally dominating gravitational center e8-N. The east-west symmetry in the possibly cometary B-field morphology in e8-S is not completely preserved in $\sin \omega$. This is likely because the dominating mass, e8-N, is located off the north-south axis. Overall, e8-S is close to maximally resisting gravity in its center (with $\sin \omega \sim 1$). At its western and eastern sides, local gravity is aligned with the B-field, hinting that e8-S can accrete material from the two sides. We note that, although showing maximum B-field effectiveness in the center, this does not yet mean that the B-field is dominating over gravity.

W51 North shows varying $\sin \omega$ structures in every core, with an overall average of 0.47 and a standard deviation of 0.30. The most massive eastern core (N1) displays small values around ~ 0.1 to 0.2 in a fan-like opening along a northeast-southwest axis. This area precisely overlaps with the polar regions of the possible hourglass field structure in this core (panel (h) in Figure 2). The very small values in $\sin \omega$ indeed suggest, as expected, that gravitational infall / collapse can easily proceed along this direction, and that the B-field

is here mostly only channeling material. In contrast to that, along the northwest-southeast axis – where the B-field is more pulled in – $\sin\omega$ is reaching maximum values close to one, indicating maximum field resistance. The next massive core to the west (N2, centered around R.A. offset $0''$) reveals another fan-like low $\sin\omega$ area in the west with gradually growing values at its eastern end. As outlined in Section 3.3 this can explain a scenario where infall / collapse can occur locally in the western zone while the eastern end starts to feel the gravitational pull by the more massive core N1 to the east, leading to a gradual bending of the field lines away from N2. This gradual bending then leads to a transition zone in between N1 and N2 where gravity and field segments are misaligned (hence, large $\sin\omega$ values), before they are aligned again in the gravitationally dominated zones in N1. The remaining two cores in the west around R.A. offset $-2''$ (N3) and R.A. offset $-3''$ (N4) display more complicated and finer structures. A possible feature is that small $\sin\omega$ values are typically found in the upper (northern) and lower (southern) mid-planes of the cores, while most maximum values appear along an east-west axis. This reflects that many field segments show a prevailing north-south orientation, which makes them being closely aligned with gravity in many places. The exceptions are the mid-planes, in particular the eastern and western ends of N3, the western end of N4, and the connecting bridge between N3 and N2 where the B-field experiences a competition between gravitational pull towards N3 and pull towards N2.

Note that $\sin\omega$ is different from the magnetic field-to-gravity force ratio, Σ_B , in our earlier analyses (Koch, Tang & Ho 2012a,b, 2013; Koch et al. 2014). Σ_B measures the local ratio between magnetic field force and gravity (in a range between zero to larger than one) by *solving* Equation (2), identifying the local direction of gravity and the field tension in an observed map. It, thus, compares and quantifies, in an absolute sense, the relative importance between magnetic field and gravity. Solving Equation (2) is based on the additional assumption of identifying an observed emission gradient direction with the inertial term in the MHD force equation. Appropriateness and possible uncertainties of this assumption are discussed in detail in Koch, Tang & Ho (2013). $\sin\omega$ is not relying on solving Equation (2). It merely projects the field force onto the local gravity direction, and it is, thus, free of the above assumption. Its shortcoming is that it can only capture the zones where gravity is clearly dominating over the B-field, i.e., where the B-field is dynamically unimportant ($\sin\omega \sim 0$ or small). For larger values, $\sin\omega \sim 1$, the absolute field strength becomes relevant for a quantitative absolute comparison against gravity. A detailed comparison between $\sin\omega$ and Σ_B , together with maps for the field strength B , will be presented in a forthcoming work. An initial comparison is showing a close structural resemblance between $\sin\omega$ - and Σ_B -maps. Since projection effects cancel out or are minimal for Σ_B – because Σ_B is the ratio of two forces with each force direction being subject to the same or similar inclination angle

(Koch, Tang & Ho 2012a) – this close resemblance argues for $\sin \omega$ being able to distinguish between zones of minimal and maximal B-field effectiveness without any significant bias due to unknown projection effects.

On a final speculative note, we stress that $\sin \omega$ is clearly not random. Moreover, within zones of low field effectiveness (small $\sin \omega$ values), there are channels with $\sin \omega \sim 0$ (Figure 9). Many of these channels appear in magnetic field convergence zones. In these *magnetic channels*, gravity can act unimpededly. If this is the case, this would indicate that along certain directions, infall and collapse can proceed in free-fall time while in other zones they are significantly slowed down or even completely brought to a halt. This interpretation is, however, at or already beyond the limit of the current resolution. Whether this speculative scenario indeed is correct, needs to be further probed with even higher-resolution data. If correct, the existence of a network of magnetic channels might have an interesting implication for the star formation rate. Hypothesizing a channel width of $\sim 0''.15$ (about half of our synthesized beam leading to a marginal detection), one such channel from the rim to the center would comprise about 0.4% of the entire volume of a $2''$ - diameter sphere as, e.g., in W51 e2. A network of 10 channels would then reduce the star formation rate to 4%, assuming that the entire mass inside the channels ($\sin \omega \sim 0$) is converted into stars, and that all the material outside ($\sin \omega$ large) is held back by the B-field. Checking observed star formation rates against future high-resolution B-field structures might hence also provide a test to further probe the $\sin \omega$ tool.

4.3. Comparing to Larger Scales: B-field and Polarization Properties in the pc-Scale Envelope

While the high-resolution ALMA data are making the small-scale dynamics visible in the B-field morphologies, a remaining key question is how the larger W51 e2, and the more elongated and filamentary e8 and W51 North are formed in a first place. To that purpose, we are here additionally comparing unpublished SMA data on larger scales that also detect the polarized emission on the bridge between e2 and e8, and in the more outer peripheral regions towards e2 and e8 (Figures 1, 2). A detailed analysis of the dynamics along the e2/e8 bridge is presented in Koch et al. (2017).

The W51 e2/e8 complex is connected with a bridge where the B-field segments appear to be bending away from e8 and gradually more directed towards e2 (panel (a) in Figure 2). Beyond a distance of about one beam size from the e2 and e8 peaks, the majority of the B-field segments starts to display a prevailing east-west orientation. The outer peripheral zones, thus, clearly reveal field orientations that are perpendicular to the north-south axis

of e2/e8, likely probing accretion scales that are very different from the inner much denser regions where the field structures likely start to be shaped by gravity. The histogram of B-field orientations - capturing the larger envelope on a ~ 0.5 pc scale – reflects this with a peak around 90° , i.e., east-west orientation (Figure 10, left panel). Histograms for the resolved cores at a ~ 5 mpc scale spread out over the full range in PA from 0 to 180° , indicating a change from a single prevailing orientation to a more uniform and broader distribution that stands for a more azimuthally symmetrical field configuration. While e8 is fairly uniform, e2 additionally shows a peak around $\sim 30^\circ$ which coincides with the orientation of magnetic field and core major axis already imprinted on the larger scale (dotted square in panel (a) in Figure 2), about $\sim 30^\circ$ off the north-south axis.

W51 North shows a similar scenario. The SMA observations with a coarser resolution around $2''$ (panel (f) in Figure 2) show one dominating core in an extended envelope along an east-west direction. At the R.A. of the core, field segments are north-south aligned, perpendicular to the source’s longer axis. Further to the west, B-field orientations are gradually bending, pointing towards the main peak. This is seen in the histogram with two separate groups around ~ 0 to 40° and around $\sim 120^\circ$ (Figure 10, right panel). The ALMA data (panel (h) in Figure 2), resolving the individual cores on a ~ 5 mpc scale, again show orientations spreading over the full PA range. Their distribution reflects again azimuthally symmetrical field configurations, with one peak around $\sim 30^\circ$ which results from the main core that appears to be rotated by $\sim 30^\circ$ with respect to the larger-scale north-south orientation.

In conclusion, for both e2/e8 and North, denser cores (e2, e8, and a chain of cores in North) appear to form along an axis perpendicular to the larger envelope-scale B-field. Their most massive cores (e2 and N1) have their B-fields oriented close to the envelope-scale field, with offsets around $\sim 30^\circ$. However, when further zooming in with higher resolution, B-field configurations generally are much more azimuthally symmetrical with further substructures that are likely decoupled from the larger-scale B-field and governed by their own dynamics. In general, the field configurations seen with the SMA on envelope scales are suggestive for a scenario where the B-field is channelling material from east and west (W51 e2/e8) and from north and south (W51 North, Tang et al. (2013)) to a mid-plane. The higher resolution SMA and ALMA data, indeed, confirm the locations of the denser cores to be aligned along a north-south (W51 e2/e8) and east-west (W51 North) axis.

An analysis analog to Section 4.1 for the SMA envelope-scale data shows similar trends. The local B-field dispersion \mathcal{S} (Figure 11) is picking up the locations where the field is changing from a rather uniform orientation (east-west in e2/e8 and north-south in North) to gravitational pull-in (northern and southern end in e2, southern end in e8, and western

end in North). Features in absolute polarization I_p are also seen at this resolution with two maxima in both e2 and e8 off their Stokes I peak positions, and with one maximum in North, west of its peak (Figure 11). Relative polarization percentages $p = I_p/I$ are – similar to the ALMA data – up to about 10% with maximum values at the lowest Stokes I contours. This confirms the p vs I anti-correlation also on the ~ 0.5 pc envelope scale (Figure 12, left panels). The only noticeable difference in this comparison with ALMA is the much more scattered \mathcal{S} vs p relation, indicating no correlation between these two observables on this scale in these sources (Figure 12, right panels).

5. Summary and Conclusion

We are presenting the first ALMA continuum polarization observations towards the high-mass star-forming regions W51 e2, e8, and North in Band 6 (230 GHz) with a resolution of $0''.26$. We further propose a diagnostic – the angle ω between the local magnetic (B) field orientation and the local gravity direction – as a way to assess the effectiveness of the B-field to oppose gravitational pull. Our main results are summarized in the following.

1. *Polarization Structures.* Polarized emission is clearly detected with ALMA across all three sources W51 e2, e8, and North. Polarization holes in the earlier SMA data are resolved, implying that such holes and depolarization zones can be signposts for more detailed or finer underlying B-field structures. The absolute polarized emission I_p shows complicated structures that do not simply correlate or anti-correlate with total Stokes I . Polarization percentages p are measured from around 0.1% to 10%. While all three sources reveal an anti-correlation between p and I with slopes around -1 , this anti-correlation shows a large scatter of almost an order of magnitude. This suggests additional physics that is not yet captured in this simple anti-correlation. SMA observations with $\theta \sim 2''$ also show a p vs I anti-correlation with similar slope and range in polarization percentage, but with a possibly smaller scatter.
2. *Magnetic Field Morphologies.* The B-field structures in all three regions are organized, coherent and connected. Additionally, detailed new substructures are resolved, revealing cometary B-field morphologies in satellite cores, convergence zones with symmetrical B-field structures, and possibly streamlined B-field morphologies. Many of the cores display structures that resemble gravitationally bent or pulled-in field lines at one end of the core, while field lines at the other end of the core appear to be dragged away towards the neighbouring next more massive core. This might support a scenario where local collapse can start in a small core while this core as an entity is dragged towards

the next larger gravitational center. The larger envelope-scale B-field morphologies, captured with the SMA $\theta \sim 2''$ observations, reveal prevailing field orientations perpendicular to the direction of the aligned higher-resolution ALMA cores. The bridge between W51 e2 and e8 reveals field lines that are gradually more bent towards the more massive e2.

3. *Magnetic Field Dispersion and Convergence Zones.* Similar to larger-scale observations by *Planck* and BLASTPol, a connection between the local B-field dispersion \mathcal{S} – capturing by how much the local field orientation varies with respect to its surrounding – and polarization percentage is also seen in the high-resolution ALMA data. In particular, a close spatial coincidence between lowest polarization percentages p and largest dispersions \mathcal{S} is evident in magnetic field convergence zones, where symmetrical B-field structures appear to converge from two sides. These convergence zones always also have smallest absolute polarized emission I_p . The drop in both I_p and p towards zones of growing \mathcal{S} can be interpreted as the cancellation of polarization signal due to rapidly changing field structures that are still not resolved.
4. *Local Magnetic Field Effectiveness Opposing Gravity.* The direction of the local B-field tension force can be projected onto the local direction of gravity by means of the measurable angle ω between a B-field orientation and local gravity. In this way, $\sin \omega$ measures the fraction of the field tension force that can work against gravity. Maps of $\sin \omega$ for all three sources W51 e2, e8, and North are not random but present organized patterns. Zones where $\sin \omega$ is small (gravity and B-field nearly aligned) indicate that the B-field is very ineffective in slowing down gravity. Any motion driven by gravity can proceed with little or almost no obstruction from the B-field. For regions with larger $\sin \omega$ values the absolute field strength and gravity need to be known to quantify the role of the B-field. Narrow sectors with $\sin \omega \sim 0$ lead to the speculation of magnetic channeling where infall and collapse could proceed in free-fall time.

Facilities: ALMA, SMA.

The authors thank the referee for valuable comments and suggestions that further improved this manuscript. This paper makes use of the following ALMA data:

ADS/JAO.ALMA#2013.1.00994.S. ALMA is a partnership of ESO (representing its member states), NSF (USA) and NINS (Japan), together with NRC (Canada), MoST and ASIAA (Taiwan), and KASI (Republic of Korea), in cooperation with the Republic of Chile. The Joint ALMA Observatory is operated by ESO, AUI/NRAO and NAOJ. PTPH acknowledges support from the Ministry of Science and Technology (MoST) in Taiwan through grant MoST

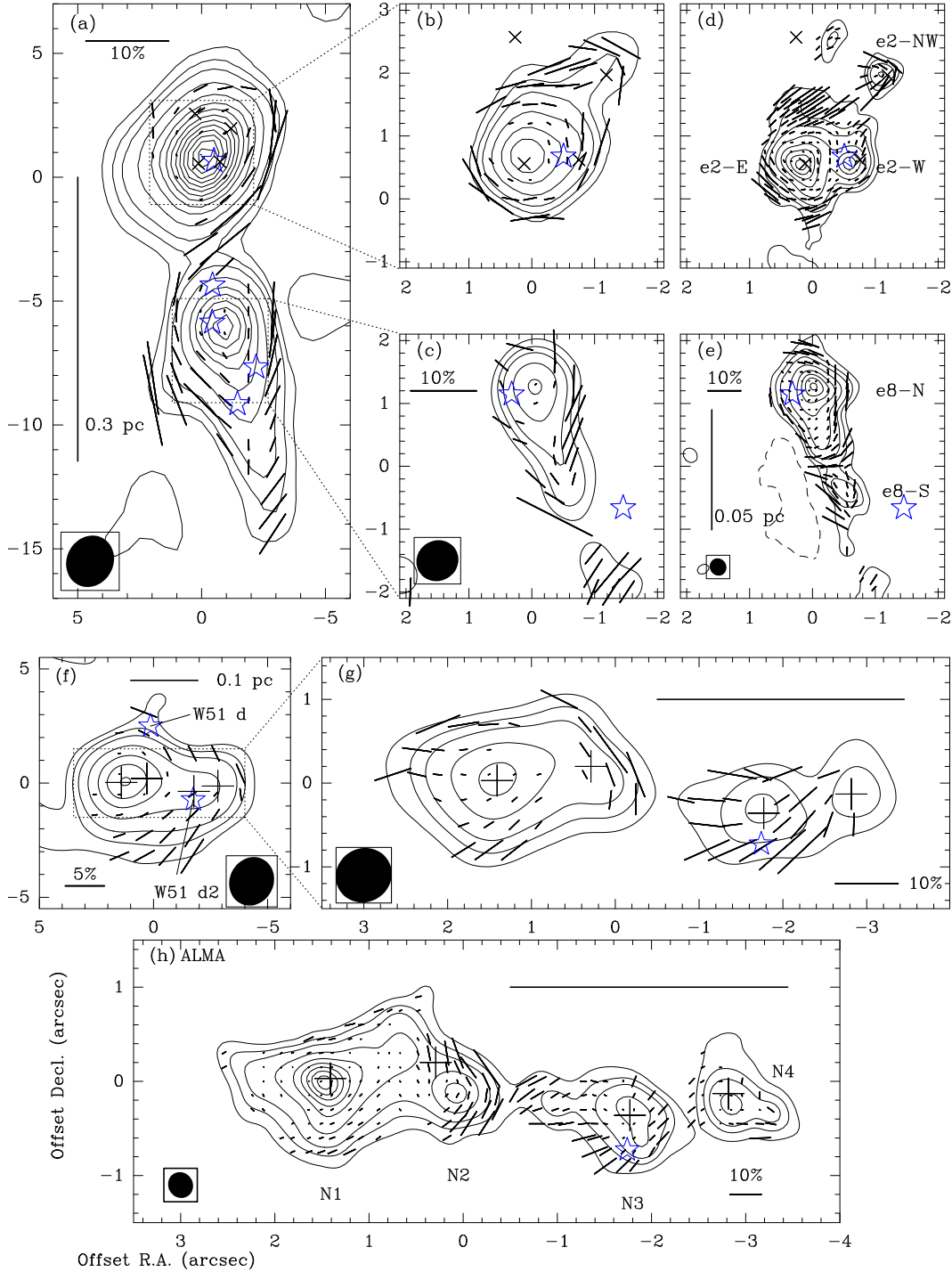


Fig. 1.— Polarization maps of W51 e2, e8, and W51 North with various angular resolutions from ALMA and the SMA. Contours are Stokes I dust continuum intensity. Polarization orientations are displayed with their lengths scaled with polarization percentage $p = I_p/I$. Contours are 3, 6, 10, 20, 35, 50, 65, 80, 95... $\times\sigma$, where 1σ is 75 mJy/beam in panel (a), 60 mJy/beam in panel (b) and (c), 6 mJy/beam in panel (d) and (e), 140 mJy/beam in panel (f), and 90 mJy/beam in panel (g). Contours in panel (h) are identical to panel (d) and (e) but 1σ is 1.4 mJy/beam. Panel (a) and (f): SMA observations with $\theta \sim 2''$ at 345 GHz probing larger envelope scales, revealing the connection between W51 e2 and e8 in panel (a) and the W51 North region in panel (f). Panel (b), (c), and (g): SMA observations with $\theta \sim 0''.7$ at 345 GHz towards W51 e2 in panel (b), W51 e8 in panel (c) (images adopted from Tang et al. (2009)), and W51 North in panel (g) (image adopted from Tang et al. (2013)). Panel (d), (e), and (h): ALMA observations in Band 6 at 230 GHz with $\theta \sim 0''.26$ towards W51 e2 in panel (d), W51 e8 in panel (e), and W51 North in panel (h). Crosses in the panels (a), (b) and (d) mark the known sub-mm sources W51 e2-E, e2-W, e2-NW and e2-N, counter-clockwise around the continuum peak. Pluses in the panels (f), (g), and (h) mark the known sub-mm sources SMA1, SMA2, SMA3 and SMA4 from east to west. N1 to N4 label the clearly resolved peaks in the ALMA observations. Blue stars indicate UCHII regions. Synthesized beams for each observation are shown with black filled ellipses. Polarization segments are gridded to and displayed at half of the synthesized beam resolution.

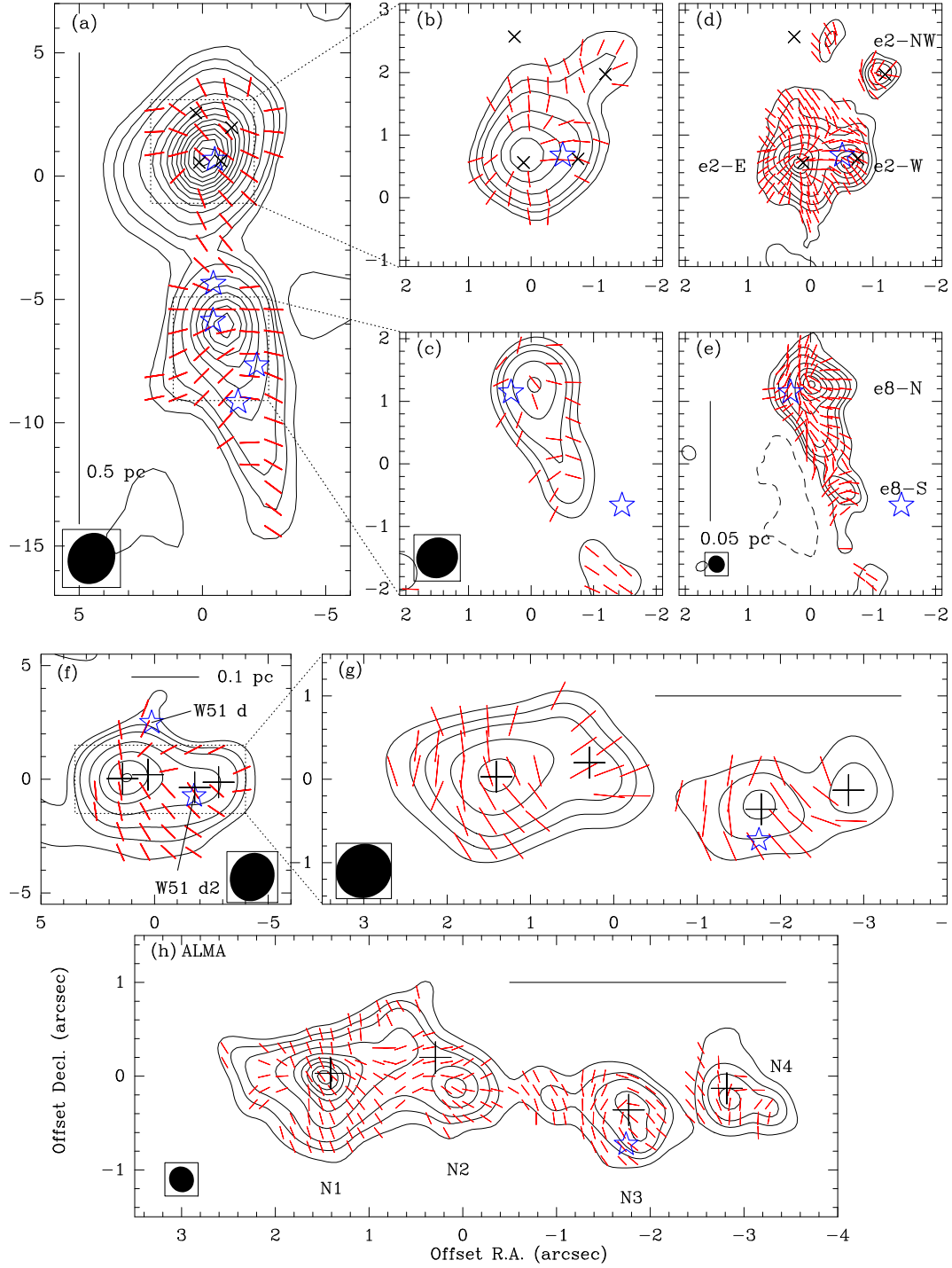


Fig. 2.— Identical to Figure 1 but with magnetic field orientations shown with red segments. B-field orientations are rotated by 90° with respect to the detected polarization orientations in Figure 1.

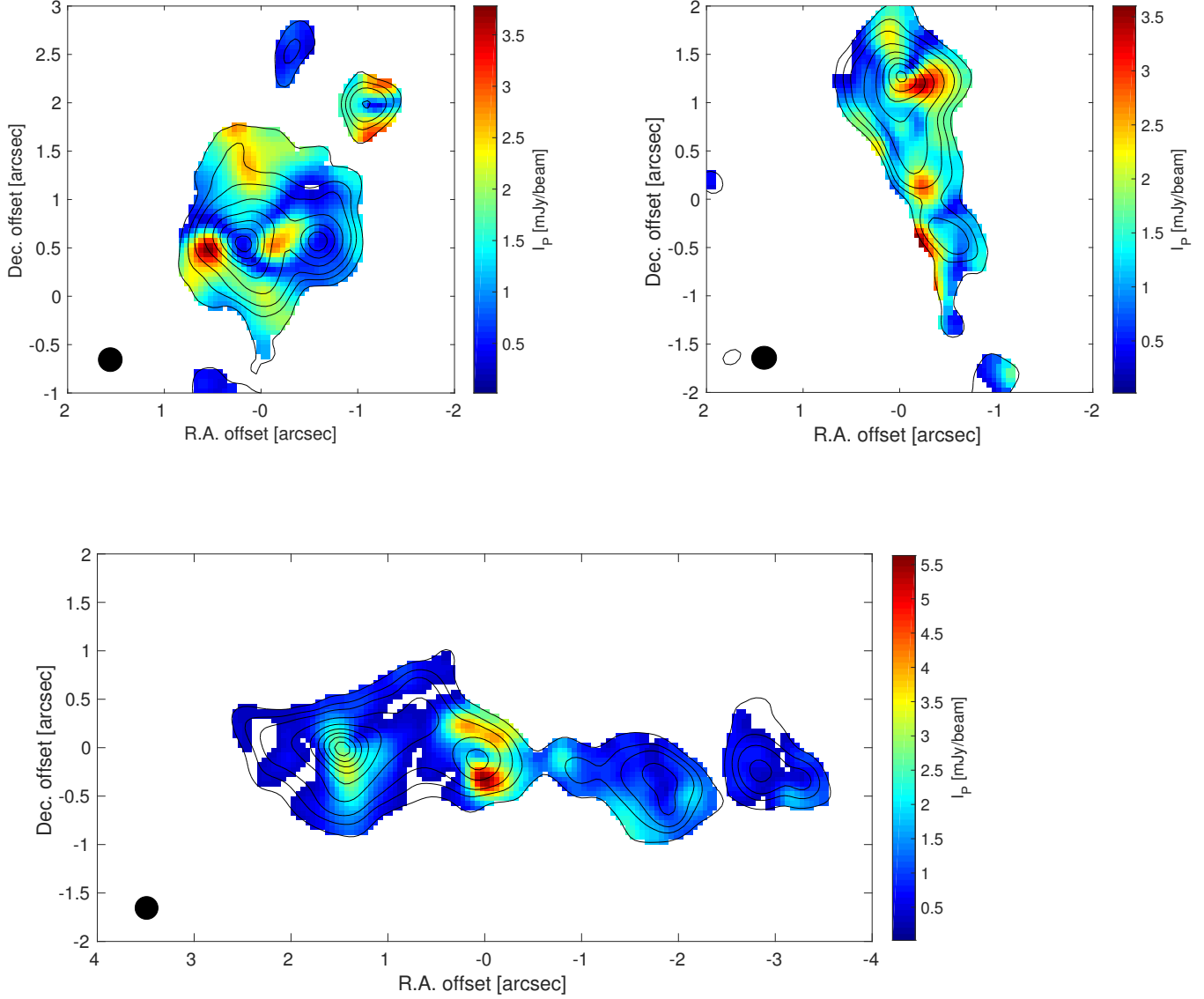


Fig. 3.— Polarized emission I_p for e2 (top left), e8 (top right) and North (bottom). Contours are dust continuum with levels as described in Figure 1, color scale is in units of mJy/beam for I_p . Note: I_p is reproduced from the ALMA maps in Figure 1 and for a better visual impression and display of features, the data are additionally overgridded and shown at five times the synthesized beam resolution. Synthesized beams are shown with black filled ellipses.

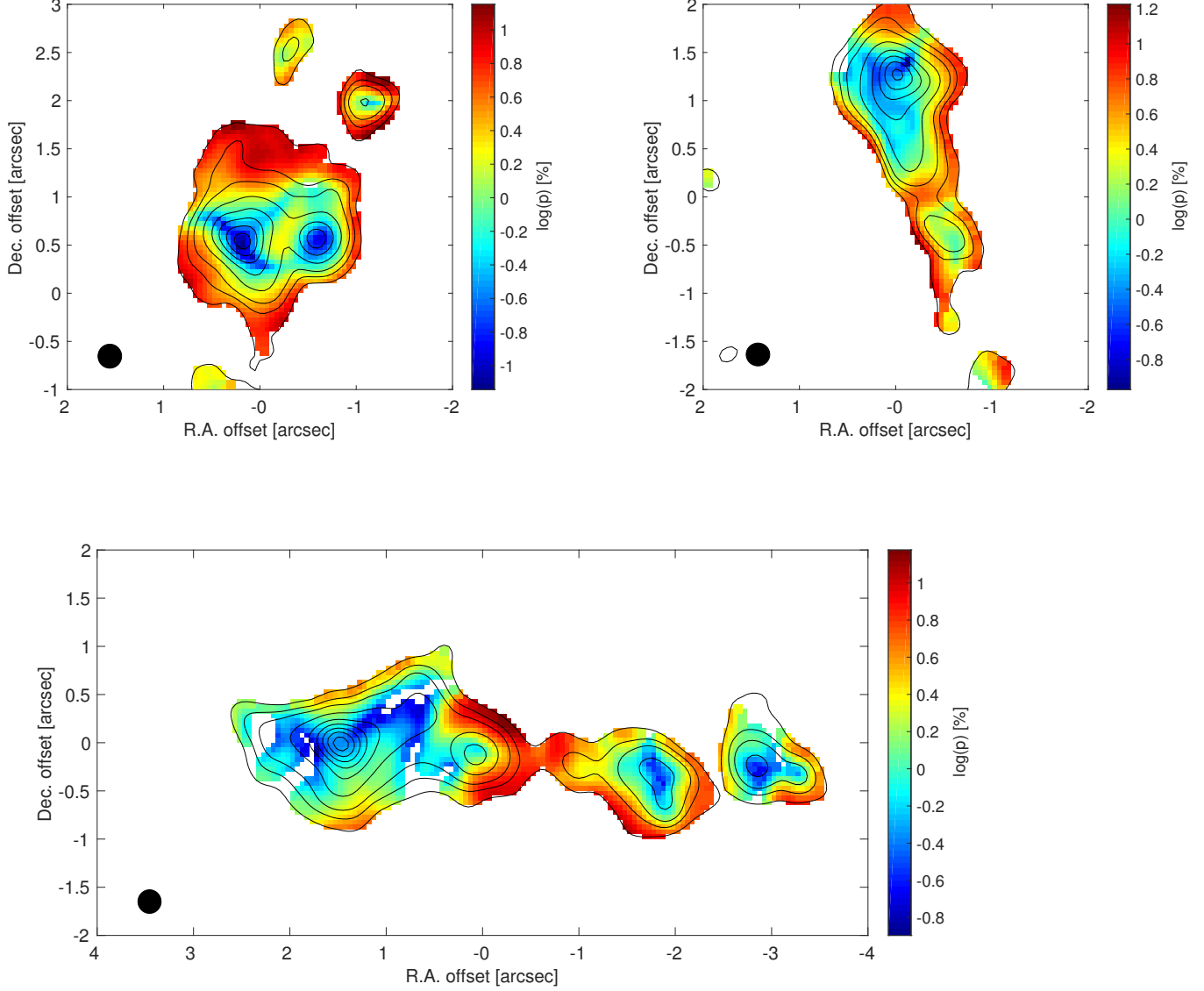


Fig. 4.— Polarization percentages $p = I_p/I$ for e2 (top left), e8 (top right) and North (bottom). Color scale is $\log(p)$. Note: Identical to Figure 3, the data are overgridded and shown at five times the synthesized beam resolution. p is extracted from the ALMA maps in Figure 1 where it is encoded in the lengths of the polarization segments. Synthesized beams are shown with black filled ellipses.

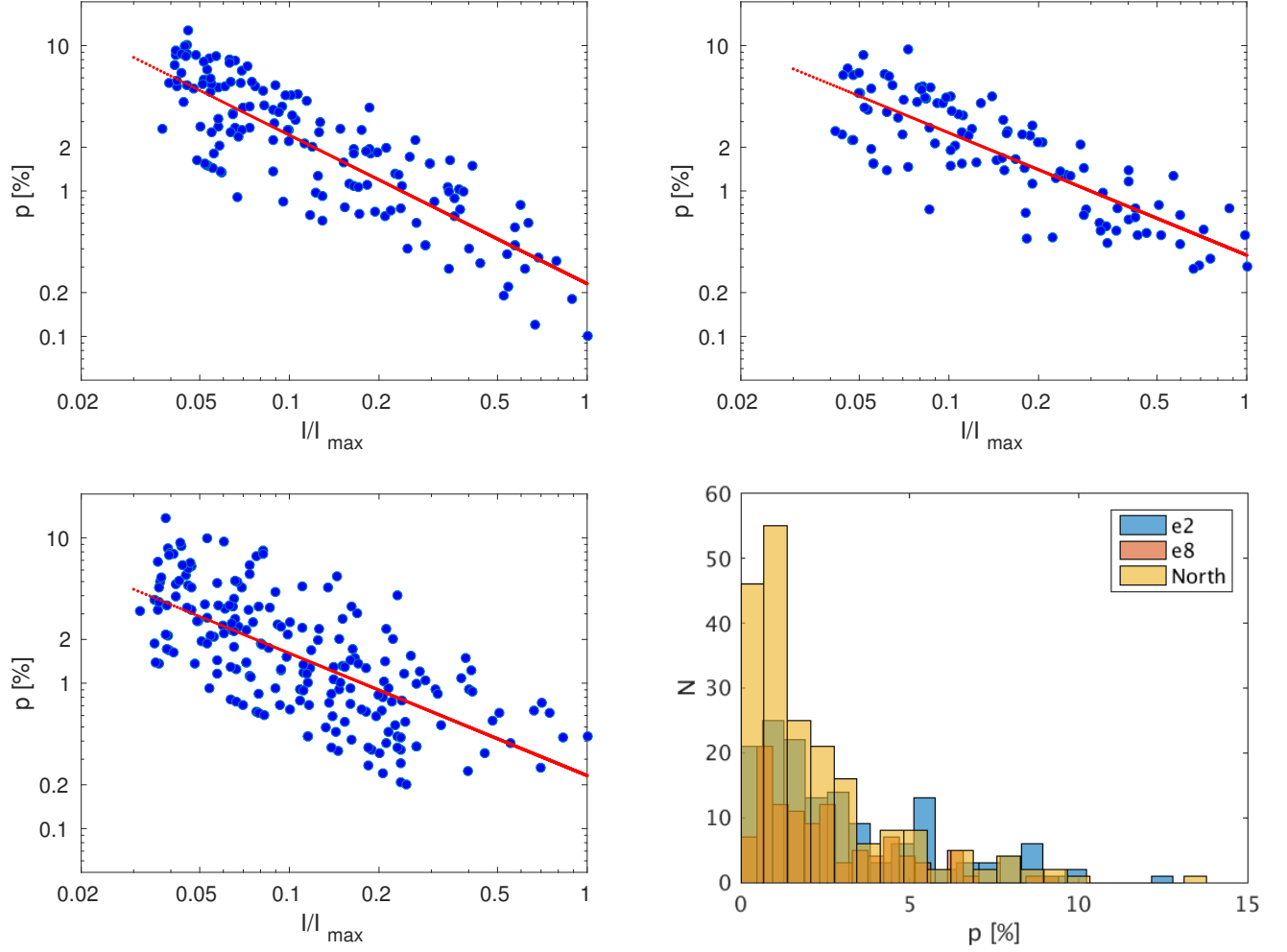


Fig. 5.— Polarization percentage $p = I_p/I$ versus Stokes I , normalized to I_{max} , for e2 (top left), e8 (top right), and North (bottom left). Unlike the overgridded data displayed in Figure 4, the data here are extracted from maps gridded to only half of the synthesized beam resolution (panels (d), (e), and (h) in Figure 1). The red solid lines are the best-fit power laws with indices -1.02 (e2), -0.84 (e8), and -0.84 (North). Bottom right panel: histograms of polarization percentages p . Averages and standard deviations are 3.1% and 2.2% , 2.5% and 2.0% , and 2.3% and 2.3% for e2, e8, and North. Maximum and minimum polarizations are 13% and 0.1% (e2), 9% and 0.3% (e8), and 14% and 0.2% (North).

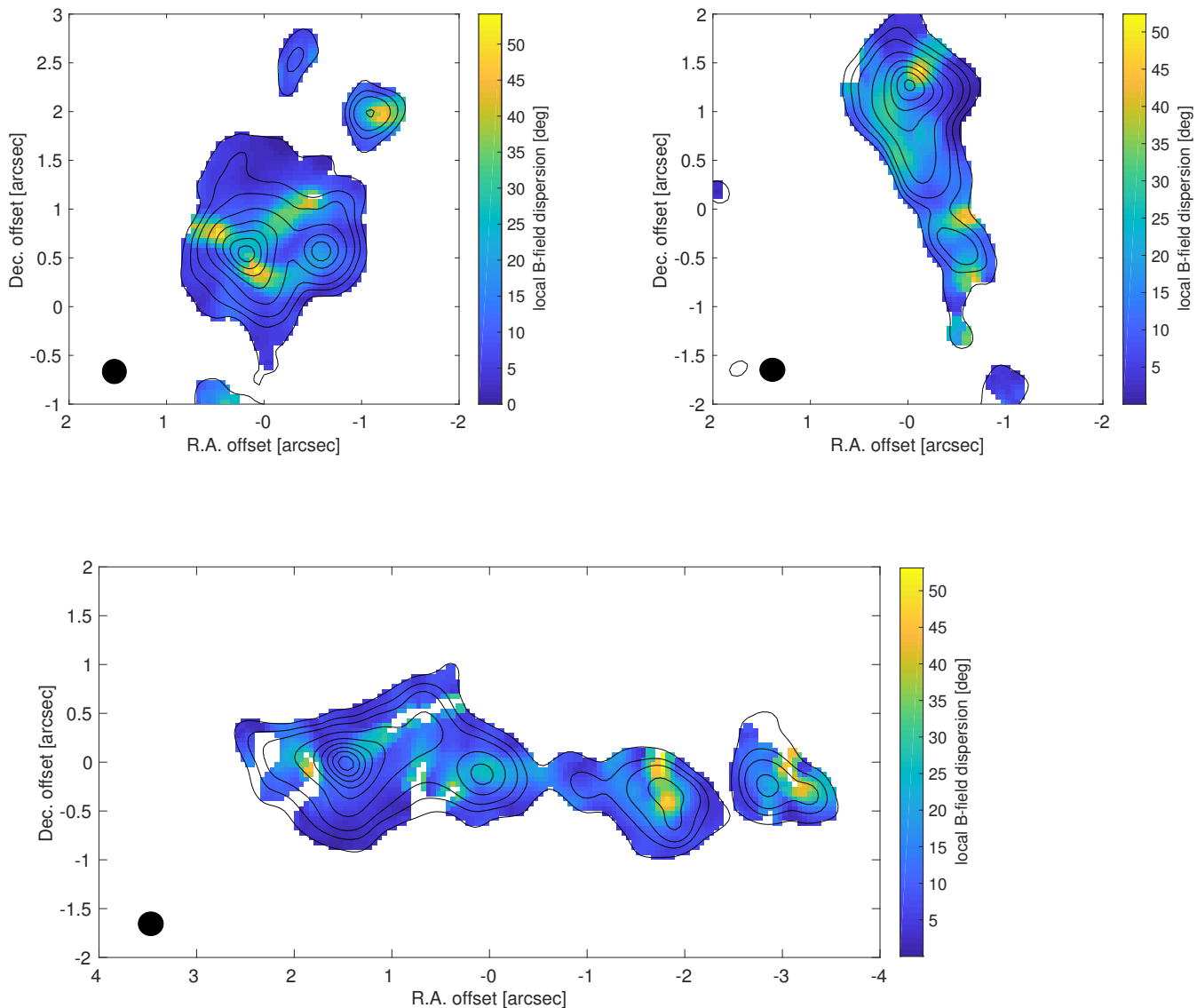


Fig. 6.— Local magnetic field dispersion \mathcal{S} (color scale in units of degrees, for radius $r_{disp} = 0''.2$) overlaid on dust Stokes I contours for e2 (top left), e8 (top right), and North (bottom). Note: Identical to the Figures 3 and 4, for a better visual impression, the data are overgridded and shown at five times the synthesized beam resolution. Synthesized beams are shown with black filled ellipses.

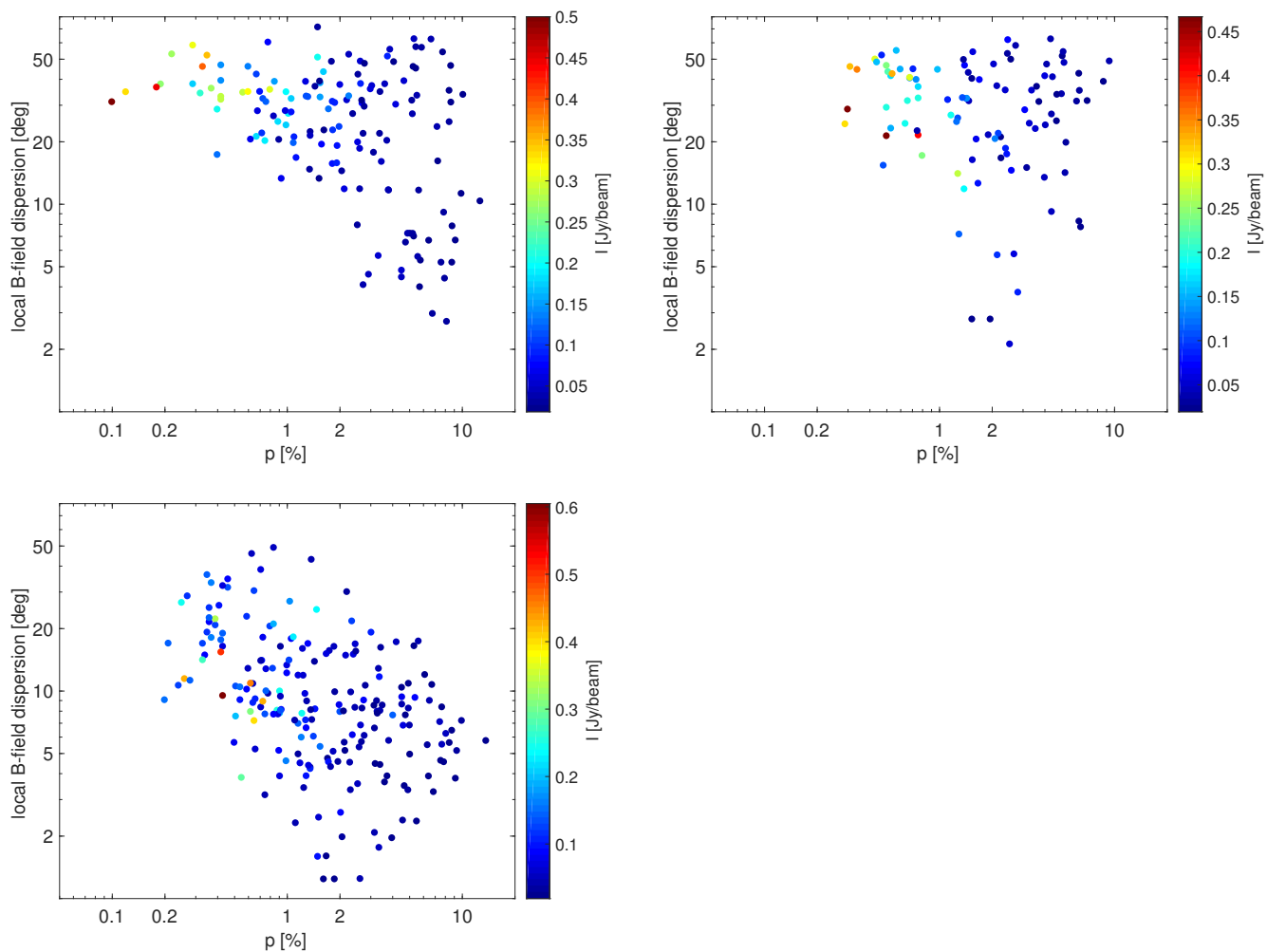


Fig. 7.— Local magnetic field dispersion \mathcal{S} ($r_{disp} = 0''.2$) versus polarization percentage p for e2 (top left), e8 (top right), and North (bottom). Stokes I emission is color-coded. Unlike the overgridded data displayed in Figure 6, data here are extracted from maps gridded to only half of the synthesized beam resolution.

Name	R.A. (J2000)	Decl. (J2000)	Size (")×(")	Flux (Jy)
W51 e2-E	19:23:43.96	14:30:34.56	0.64×0.54	2.54
W51 e2-N	19:23:43.93	14:30:36.53	0.52×0.11	0.10
W51 e2-W	19:23:43.91	14:30:34.59	0.44×0.39	1.04
W51 e2-NW	19:23:43.88	14:30:35.98	0.28×0.22	0.22
W51 e8-N	19:23:43.90	14:30:28.14	0.81×0.51	2.65
W51 e8-S	19:23:43.87	14:30:26.63	0.67×0.31	0.34
W51N1	19:23:40.05	14:31:5.47	0.73×0.51	2.88
W51N SMA2-E	19:23:40.00	14:31:5.73	0.88×0.73	1.49
W51N2	19:23:39.96	14:31:5.41	0.62×0.41	0.96
W51N3	19:23:39.83	14:41:5.11	0.74×0.52	0.89
W51N4	19:23:39.75	14:41:5.26	0.68×0.45	0.59

Table 1: Cores in W51 e2, e8, and North, identified from dust continuum in Figure 1. Positions, deconvolved sizes, and integrated flux densities are all measured at 230 GHz in Band 6 with ALMA .

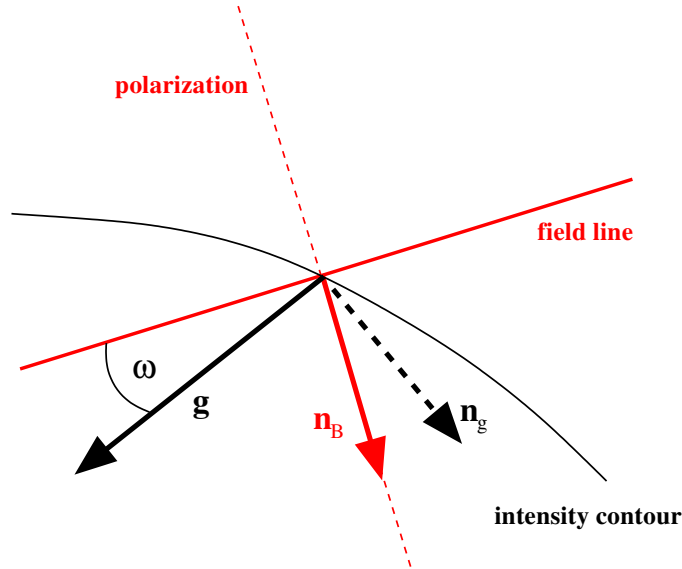


Fig. 8.— Illustration of the angle ω that measures the deviation between the magnetic field orientation (in the case of submm dust polarization rotated by 90° from the originally detected polarization orientation) and the direction of local gravity \mathbf{g} . \mathbf{n}_g is orthogonal to \mathbf{g} and forms an orthonormal system with it. \mathbf{n}_B is the unity vector perpendicular to a measured B-field orientation along the direction of the field tension force.

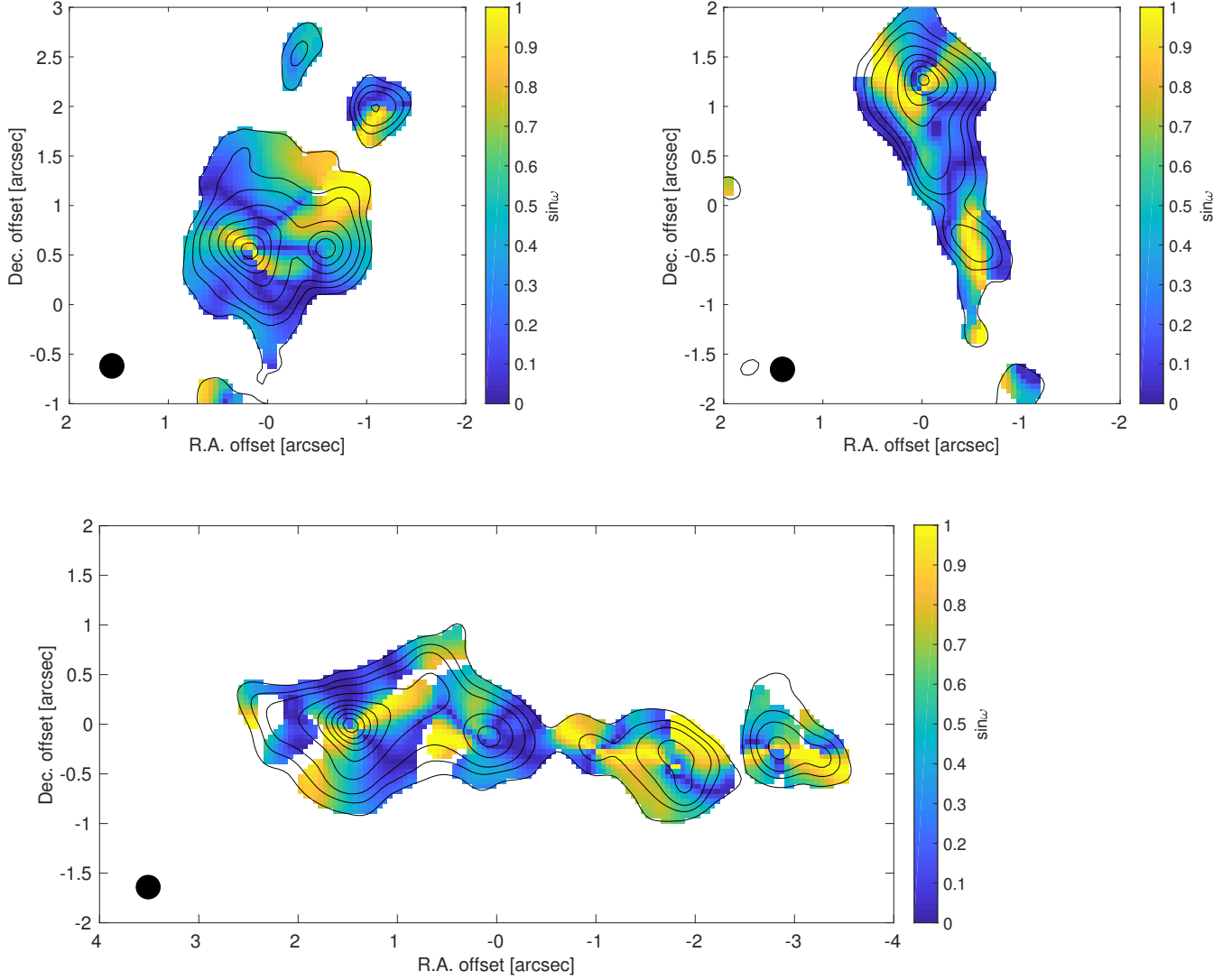


Fig. 9.— $\sin \omega$ -maps for e2 (top left), e8 (top right), and North (bottom). $\sin \omega$ is in the range between 0 and 1, where $\sin \omega \sim 0$ and small values (blue) indicate no or only minimal B-field effectiveness to oppose gravity, and $\sin \omega \sim 1$ (yellow, orange) marks zones with maximum B-field effectiveness. In the blueish zones, gravity can act most efficiently. Magnetic channels (dark blue, $\sin \omega \sim 0$) are within these zones. Identical to the Figures 3, 4, and 6, these maps are also overgridded for a sharper display of features.

105-2112-M-001-025-MY3. Y-WT is supported through grant MoST 103-2119-M-001-010-MY2. PMK acknowledges support from MoST 103-2119-M-001-009 and from an Academia Sinica Career Development Award.

REFERENCES

- Andersson, B.-G., Lazarian, A., & Vaillancourt, J. E. 2015, *ARA&A*, 53, 501
- Brown, R.D., & Cragg, D.M. 1991, *ApJ*, 378, 445
- Chandrasekhar, S., & Fermi, E. 1953, *ApJ*, 118, 113
- Cho, J., Lazarian, A. 2005, *ApJ*, 631, 361
- Chrysostomou, A., Aitken, D.K., Jenness, T., Davis, C.J., Hough, J.H., Curran, R., Tamura, M. 2002, *A&A*, 385, 1014
- Cudlip, W., Fruniss, I., King, K. J., & Jennings, R. E. 1982, *MNRAS*, 200, 1169
- Dotson, J.L., Vaillancourt, J.E., Kirby, L., Dowell, C.D., Hildebrand, R.H., & Davidson, J.A. 2010, *ApJS*, 186, 406
- Draine, B.T., & Weingartner, J.C. 1996, *ApJ*, 470, 551
- Draine, B.T., & Weingartner, J.C. 1997, *ApJ*, 480, 633
- Eisner, J.A., Greenhill, L.J., Herrnstein, J.R., Moran, J.M., & Menten, K.M. 2002, *ApJ*, 569, 334
- Etoka, S., Gray, M.D., Fuller, G.A. 2012, *MNRAS*, 423, 647
- Fish, V.L., & Reid, M.J., 2007, *ApJ*, 670, 1159
- Fissel, L.M. et al. 2016, *ApJ*, 824, 134
- Gaume, R.A., Johnstone, K.J., & Wilson, T.L. 1993, *ApJ*, 417, 645
- Genzel, R., et al. 1981, *ApJ*, 247, 1039
- Ginsburg, A., 2017, arXiv:1702.06627v1; published in *Star Formation Newsletter #290*, <http://www.ifa.hawaii.edu/users/reipurth/newsletter/newsletter290.pdf>
- Ginsburg, A., Goddi, C., Diederik Kruijssen, J.M., et al. 2017, *ApJ*, 842, 92

- Goddi, C., Henkel, C., Zhang, Q., Zapata, L., & Wilson, T.L. 2015, *A&A*, 573, A109
- Goddi, C., Ginsburg, A., & Zhang, Q. 2016, *A&A*, 589, A44
- Henkel, C., Wilson, T.L., Asiri, H., Mauersberger, R. 2013, *A&A*, 549, A90
- Hildebrand, R. H. 1988, *QJRAS*, 29, 327
- Hildebrand, R. H., Dragovan, M., & Novak, G. 1984, *ApJ*, 284, L51
- Ho, P.T.P., & Young, L.M. 1996, *ApJ*, 472, 742
- Ho, P.T.P., Moran, J.M., and Lo, K.-Y. 2004, *ApJ*, 616, 1
- Hoang, T., & Lazarian, A. 2016, *ApJ*, 831, 159H
- Imai, H., Watanabe, T., Omodaka, T., Nishio, M., Kameya, O., Miyaji, T., & Nakajima, J. 2002, *PASJ*, 54, 741
- Keto, E., & Klaassen, P., 2008, *ApJ*, 678, L109
- Koch, P.M., Tang, Y.-W., Ho, P.T.P. 2012a, *ApJ*, 747, 79
- Koch, P.M., Tang, Y.-W., Ho, P.T.P. 2012b, *ApJ*, 747, 80
- Koch, P.M., Tang, Y.-W., Ho, P.T.P. 2013, *ApJ*, 775, 77K
- Koch, P.M., Tang, Y.-W., Ho, P.T.P., Zhang, Q., Girart, J.M., Chen, H.-R.V. et al. 2014 *ApJ*, 797, 99
- Koch, P.M. et al., 2017, in preparation
- Lai, S.-P., Crutcher, R.M., Girart, J.M., Rao, R. 2001, *ApJ*, 561, 864L
- Lazarian, A. 2000, *ASPC*, 215, 69
- Lazarian, A., & Hoang, T. 2007, *MNRAS*, 378, 910
- Leahy, P. 1989, *VLA Scientific Memoranda* 161 (Socorro, NM: VLA)
- Matthews, B. C., McPhee, C. A., Fissel, L. M., & Curran, R. L. 2009, *ApJS*, 182, 143
- Morita, K.-I., Hasegawa, T., Ukita, N., Okumura, S.K., & Ishiguro, M. 1992, *PASJ*, 44, 373
- Nagai, H., Nakanishi, K., Paladino, R. et al. 2016, *ApJ*, 824, 132
- Planck Intermediate Results XIX, 2015, *A&A*, 576, A104

- Planck Intermediate Results XX, 2015, *A&A*, 576, A105
- Martin, A.H.M. 1972, *MNRAS*, 157, 31
- Matthews, B.C., McPhee, C.A., Fissel, L.M., & Curran, R.L. 2009, *ApJS*, 182, 143
- Mehring, D.M. 1994, *ApJS*, 91, 713
- Phillips, C., & van Langevelde, H.J. 2005, in *Astronomical Society of the Pacific Conference Series*, Vol. 340, 342
- Rudolph, A., Welch, W. J., Palmer, P., & Dubrulle, B. 1990, *ApJ*, 363, 528
- Sato, M., Reid, M.J., Brunthaler, A., & Menten, K.M. 2010, *ApJ*, 720, 1055
- Sollins, P. K., Zhang, Q., & Ho, P.T.P., 2004, *ApJ*, 606, 943
- Shi, H., Zhao, J.-H., & Han, J.L., 2010a, *ApJ*, 718, L181
- Shi, H., Zhao, J.-H., & Han, J.L., 2010b, *ApJ*, 710, 843
- Tang, Y.-W., Ho, P.T.P., Koch, P.M., Girart, J.M., Lai, S.-P., Rao, R. 2009, *ApJ*, 700, 251
- Tang, Y.-W., Ho, P.T.P., Koch, P.M., Guilloteau, S. & A. Dutrey, 2013, *ApJ*, 763, 135
- Wardle, J. F. C. & Kronberg, P. P. 1974, *ApJ*, 194, 249
- Westerhout, G. 1958, *Bull. Astron. Inst. Neth.*, 14, 215
- Xu, Y., Reid, M.J., Menten, K.M., Brunthaler, A., Xheng, X.W., & Moscadelli, L. 2009, *ApJ*, 693, 413
- Young, L. M., Keto, E., & Ho, P.T.P., 1998, *ApJ*, 507, 270
- Zapata, L.A., Palau, A., Ho, P.T.P., et al. 2008, *A&A*, 479, L25
- Zapata, L.A., Ho, P.T.P., Schilke, P., et al., 2009, *ApJ*, 698, 1422
- Zhang, Q., & Ho, P.T.P., 1997, *ApJ*, 488, 241
- Zhang, Q., Ho, P.T.P., & Ohashi, N., 1998, *ApJ*, 494, 636
- Zhang, Q., Qiu, K., Girart, J.M., Liu, H.-Y.B., Tang, Y.-W., Koch, P.M., et al., 2014, *ApJ*, 779, 116

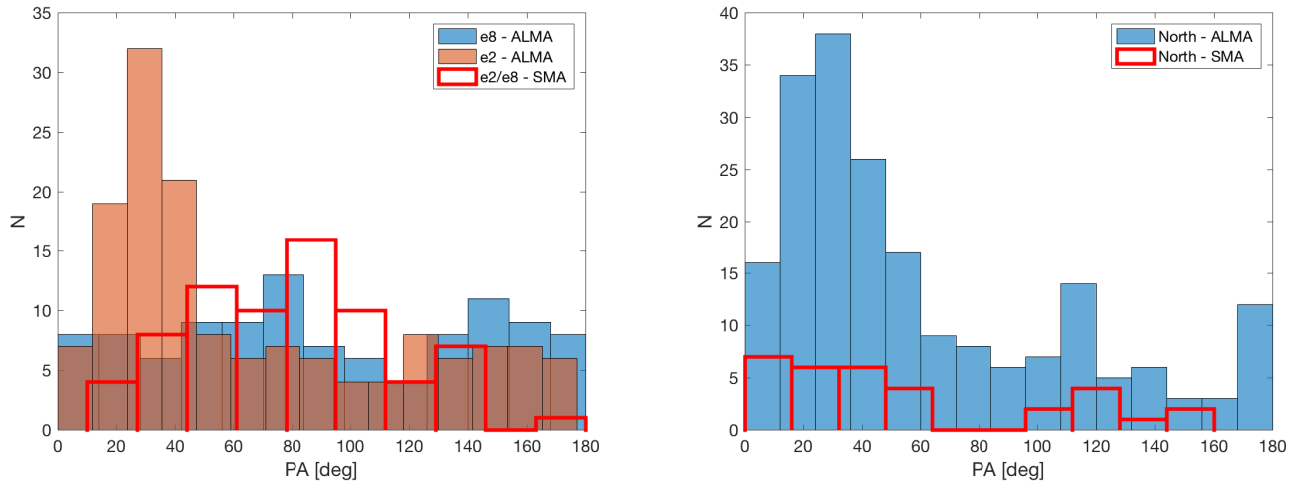


Fig. 10.— Left panel: Histograms of B-field orientations for the SMA combined e2/e8 ($\theta \sim 2''$, panel (a) in Figure 2), and the separate $\theta \sim 0''.26$ ALMA e2 and e8 (panels (d) and (e) in Figure 2). Right panel: identical but for SMA North and ALMA North.

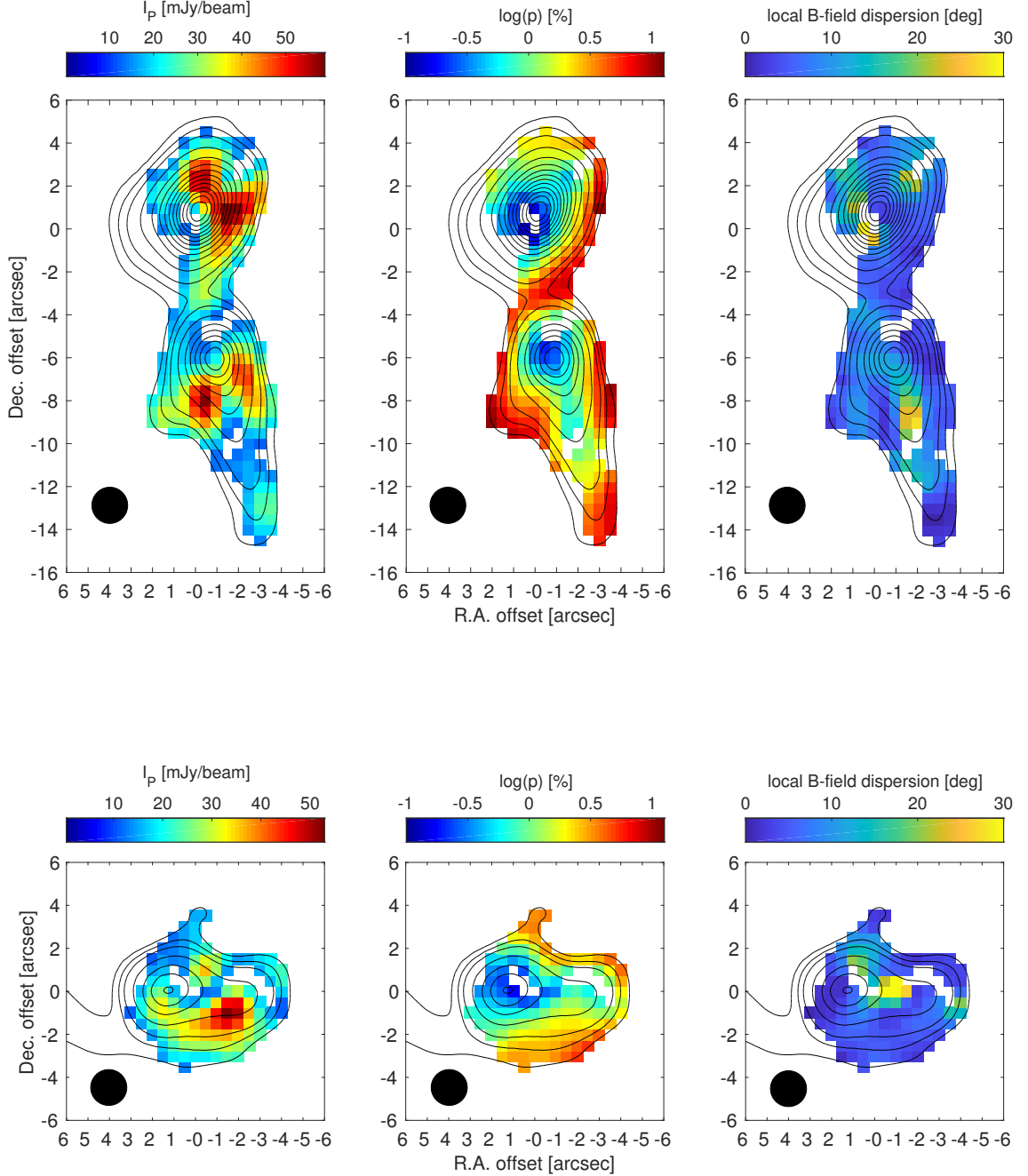


Fig. 11.— Absolute polarization I_p , polarization percentage $p = I_p/I$, and local B-field dispersion \mathcal{S} for the SMA subcompact array observations of W51 e2/e8 (upper panels) and North (lower panels) with a resolution $\theta \sim 2''$. The displayed data are overridged to $0''.5$. Contours are dust continuum with levels as described in Figure 1,

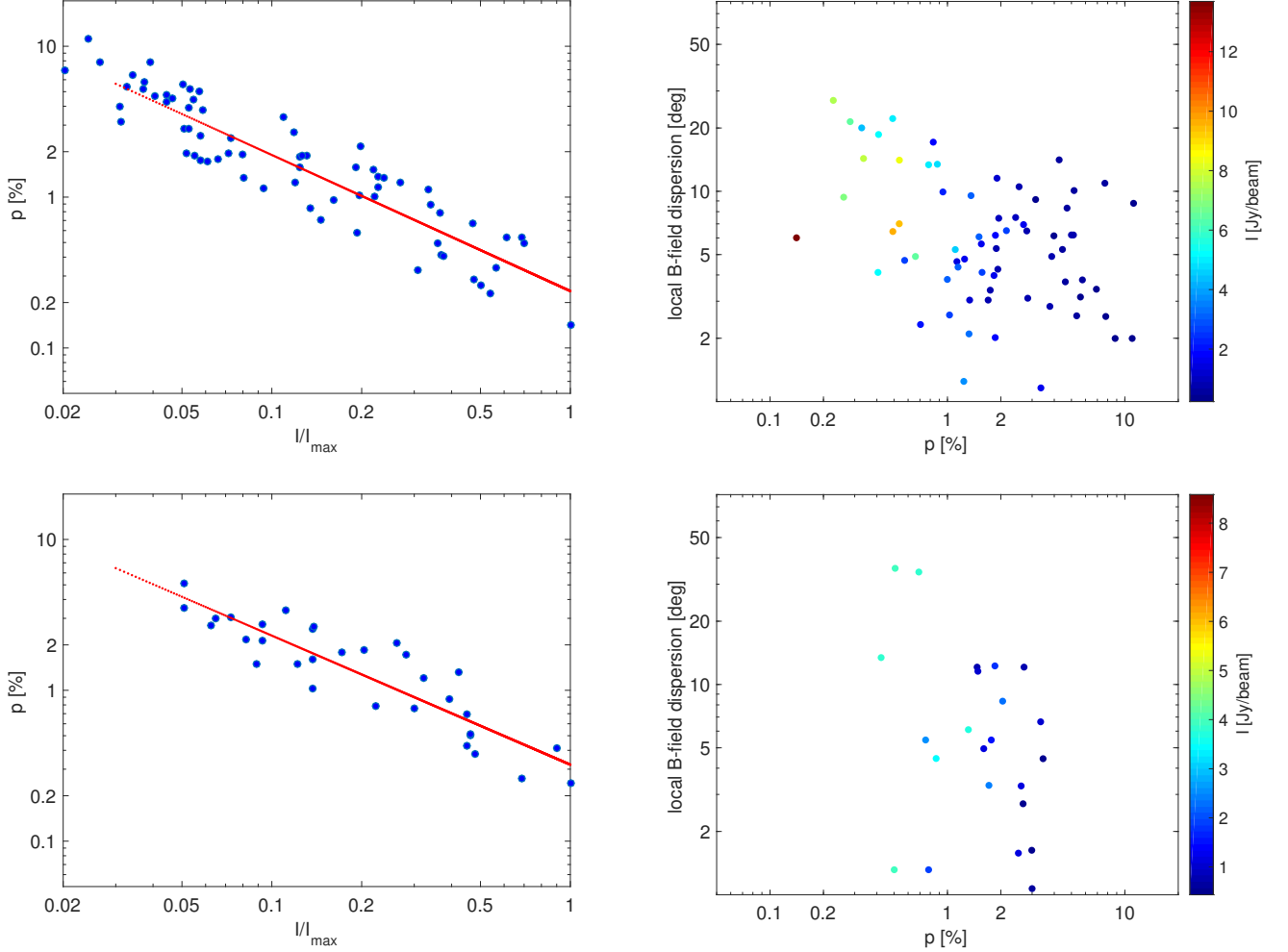


Fig. 12.— Polarization percentage $p = I_p/I$ versus Stokes I , normalized to I_{max} (left panels) and local B-field dispersion \mathcal{S} versus p (right panels) for W51 e2/e8 (upper panels) and North (lower panels) for the SMA subcompact array observations in the panels (a) and (f) in Figure 1 and 2. Unlike the overgridded data displayed in Figure 11, the data here are extracted from maps gridded to only half of the synthesized beam resolution (Figures 1 and 2). The red solid lines are the best-fit power laws with indices -0.90 (e2/e8) and -0.86 (North).

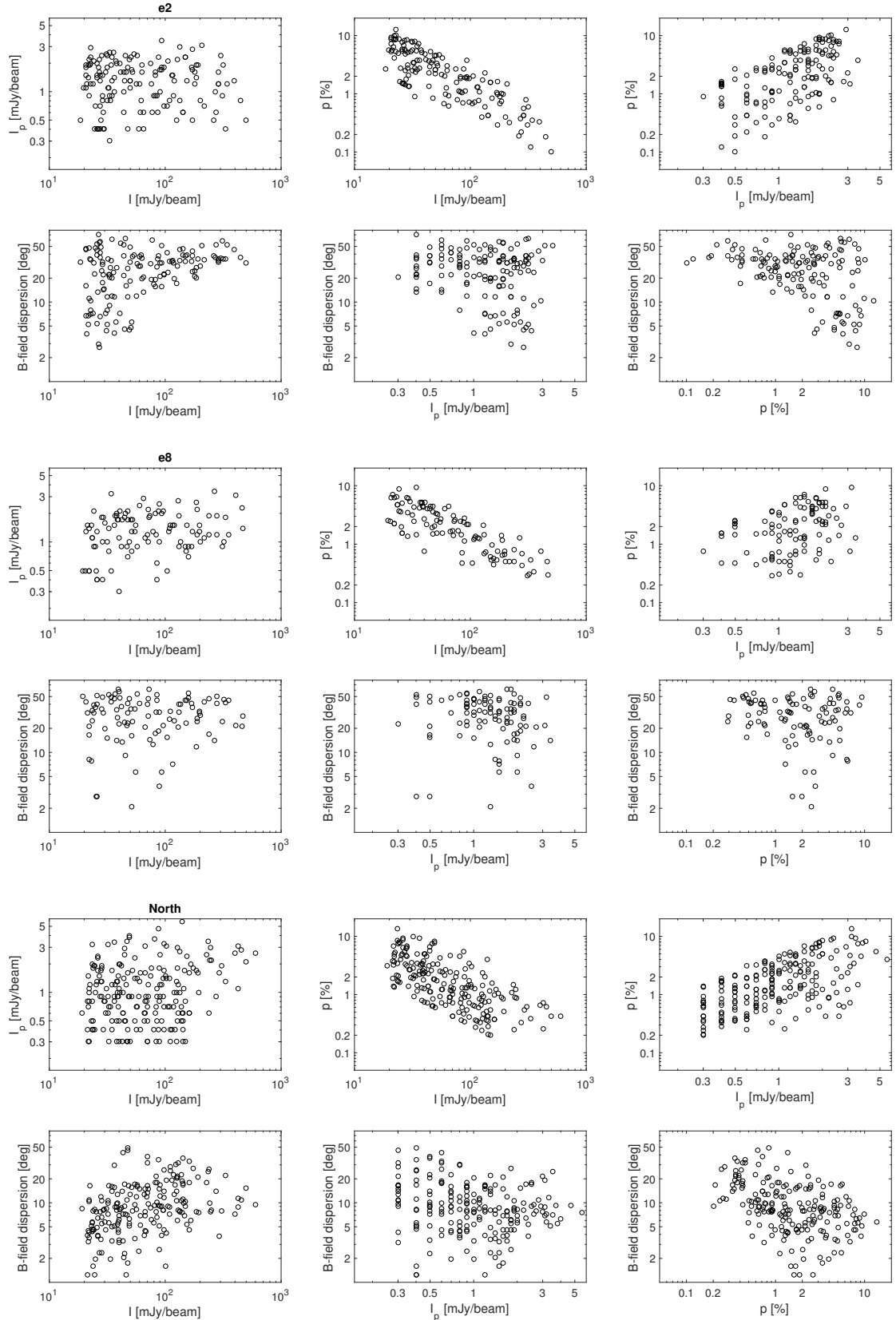


Fig. 13.— All possible correlations among Stokes I , absolute polarization I_p , polarization percentage $p = I_p/I$, and local B-field dispersion S for W51 e2 (top two rows), e8 (middle two rows), and North (bottom two rows) observed with ALMA.